Monthly Notices
of the
ROYAL ASTRONOMICAL SOCIETY
MNRAS **443,** 1231–1251 (2014) doi:10.1093/mnras/stu1198

The 6dF Galaxy Survey: Fundamental Plane data

Lachlan A. Campbell,[1⋆] John R. Lucey,[2⋆] Matthew Colless,[1,3] D. Heath Jones,[1,4] Christopher M. Springob,[1,5,6] Christina Magoulas,[1,7] Robert N. Proctor,[8] Jeremy R. Mould,[7,9] Mike A. Read,[10] Sarah Brough,[1] Tom Jarrett,[11,12] Alex I. Merson,[2,13] Philip Lah,[3] Florian Beutler,[5,14] Michelle E. Cluver[1,11] and Quentin A. Parker[1,15]

[1]*Australian Astronomical Observatory, PO Box 915, North Ryde, NSW 1670, Australia*
[2]*Department of Physics, Durham University, Durham DH1 3LE, UK*
[3]*Research School of Astronomy & Astrophysics, The Australian National University, Canberra, ACT 2611, Australia*
[4]*School of Physics, Monash University, Clayton, VIC 3800, Australia*
[5]*International Centre for Radio Astronomy Research, The University of Western Australia, Crawley, WA 6009, Australia*
[6]*ARC Centre of Excellence for All-sky Astrophysics (CAASTRO)*
[7]*School of Physics, University of Melbourne, Parkville, VIC 3010, Australia*
[8]*Observatório Nacional, Rua Gal. José Cristino 77, 20921-400 Rio de Janeiro, Brazil*
[9]*Centre for Astrophysics & Supercomputing, Swinburne University of Technology, PO Box 218, Hawthorn, VIC 3122, Australia*
[10]*Institute for Astronomy, School of Physics and Astronomy, Royal Observatory, Blackford Hill, Edinburgh EH9 3HJ, UK*
[11]*Spitzer Science Center, California Institute of Technology, Pasadena, CA 91125, USA*
[12]*Astronomy Department, University of Cape Town, Private Bag X3, Rondebosch 7701, South Africa*
[13]*Department of Physics and Astronomy, University College London, Gower Street, London WC1E 6BT, UK*
[14]*Lawrence Berkeley National Laboratory, 1 Cyclotron Road, Berkeley, CA 94720, USA*
[15]*Department of Physics & Astronomy, Macquarie University, Sydney, NSW 2109, Australia*

Accepted 2014 June 16. Received 2014 June 15; in original form 2013 October 8

ABSTRACT

We report the 6dFGS Fundamental Plane (6dFGSv) catalogue that is used to estimate distances and peculiar velocities for nearly 9000 early-type galaxies in the local ($z < 0.055$) universe. Velocity dispersions are derived by cross-correlation from 6dF *V*-band spectra with typical S/N of 12.9 Å^{-1} for a sample of 11 315 galaxies; the median velocity dispersion is 163 km s^{-1} and the median measurement error is 12.9 per cent. The photometric Fundamental Plane (FP) parameters (effective radii and surface brightnesses) are determined from the *JHK* 2MASS images for 11 102 galaxies. Comparison of the independent *J*- and *K*-band measurements implies that the average uncertainty in $X_{\rm FP}$, the combined photometric parameter that enters the FP, is 0.013 dex (3 per cent) for each band. Visual classification of morphologies was used to select a sample of nearly 9000 early-type galaxies that form 6dFGSv. This catalogue has been used to study the effects of stellar populations on galaxy scaling relations, to investigate the variation of the FP with environment and galaxy morphology, to explore trends in stellar populations through, along and across the FP, and to map and analyse the local peculiar velocity field.

Key words: galaxies: elliptical and lenticular, cD – galaxies: evolution – galaxies: fundamental parameters – galaxies: photometry – galaxies: structure.

1 INTRODUCTION

The primary goals of the 6-degree Field Galaxy Survey (6dFGS; Jones et al. 2004, 2005, 2009) were, first, to improve our knowledge of the cosmography of the nearby universe over the Southern hemisphere and, secondly, to provide a sample of ∼10 000 nearby early-type galaxies in order to study their intrinsic properties and to measure peculiar velocities via the determination of Fundamental Plane (FP) distances.

An important aspect of 6dFGS is that all observations were obtained on a single system, the UK Schmidt Telescope and the 6-degree Field (6dF) spectrograph (Watson, Parker & Miziarski

⋆E-mail: lachlan.a.campbell@googlemail.com (LAC); john.lucey@durham.ac.uk (JRL)

1998), resulting in a homogeneous spectroscopic data set. The 6dF system provided 150 optical fibres, each with a 6.7 arcsec diameter aperture, that were deployed across a field of view of nearly 6°. 6dFGS covers the entire Southern hemisphere with $|b| > 10°$. The primary galaxy sample for the 6dFGS was selected in the K_s band from the Two Micron All Sky Survey (2MASS; Jarrett et al. 2000). Near-infrared (NIR) selection means the primary sample provides a relatively unbiased (i.e. approximately mass-selected) survey of galaxies with old stellar populations in the nearby universe. Over the period of the 6dFGS observations, from 2001 to 2006, survey observations produced approximately 137 000 spectra. The 6dFGS data base (available at www-wfau.roe.ac.uk/6dfgs) contains these spectra along with 124 000 galaxy redshifts and the 2MASS photometry and images. The median redshift is 0.05 and the redshift completeness of 6dFGS is 88 per cent; full details are given in Jones et al. (2009).

As well as the galaxy redshift survey, 6dFGS had two further major aims that focused on the early-type galaxies.

The first aim was to provide an NIR-selected spectroscopic and photometric sample with which to study the FP, the scaling relation linking the velocity dispersion, effective radius and surface brightness of early-type galaxies (Djorgovski & Davis 1987; Dressler et al. 1987). The 6dFGS subsample of early-type galaxies with measured FP parameters has been used to investigate the physical origins of the FP, and its implications for galaxy formation and evolution, by exploring variations in the FP with galaxy and environmental properties, including stellar population and morphology (see Proctor et al. 2008; Magoulas et al. 2012; Springob et al. 2012).

The second aim was to compile a large homogeneous peculiar velocity catalogue derived from NIR FP distances in order to map the nearby large-scale mass distribution for cosmological studies. Peculiar velocities are a direct tracer of the underlying distribution of mass in the universe, so a combined redshift and peculiar velocity survey over the same volume can provide even better constraints on parameters of cosmological interest than a survey of redshifts alone (Burkey & Taylor 2004; Zaroubi & Branchini 2005). Several recent reconstructions of the peculiar velocity field in the Southern hemisphere have used the redshifts provided by 6dFGS (e.g. Erdoğdu et al. 2006; Lavaux et al. 2010; Lavaux & Hudson 2011).

While the first studies of FP-based peculiar velocities used velocity dispersions that were measured individually (e.g. Davies et al. 1987; Lynden-Bell et al. 1988), the advent of multi-object fibre systems dramatically improved the observing efficiency for measuring velocity dispersions, particularly when studying galaxies in rich clusters (e.g. Colless & Hewett 1987; Lucey & Carter 1988; Jorgensen, Franx & Kjaergaard 1995b). The 6dFGS peculiar velocity survey (6dFGSv) was designed to build on the success of these first fibre-based studies and provide a large set of FP peculiar velocities over the whole of the Southern hemisphere. The 6dFGSv sample was selected from the brightest (and so highest spectroscopic S/N) ellipticals, lenticulars and early-type spiral bulges in the primary 6dFGS redshift sample over the volume out to $\sim$16 500 km s^{-1}.

Here we present the 6dFGSv data set. The structure of the paper is as follows. In Section 2, we describe in detail the procedures used to determine velocity dispersions of 11 315 early-type galaxies and provide a comparison with external catalogues. In Section 3, we outline the techniques we adopted to measure point spread function (PSF) corrected FP photometric parameters (R_e and $\langle\mu_e\rangle$) from the 2MASS image tiles and demonstrate that these new NIR measurements are in excellent agreement with values previously derived from NIR and optical data. In Section 4, we describe the visual classification of the 6dFGSv galaxy morphologies, which is used to restrict the sample to those objects likely to yield reliable FP results. The construction of the 6dFGSv catalogue that is used in our FP studies is reported in Section 5. Finally, we present some brief conclusions and highlight ongoing studies in Section 6.

2 SPECTROSCOPIC MEASUREMENTS

2.1 6dF spectra and sample selection

The main characteristics of the 6dFGS, including the 6dF instrument, target catalogue construction, the allocation of fields and fibres to targets, data reduction and procedures for redshift determination, are reported in Jones et al. (2004). Briefly, 6dF uses 6.7 arcsec diameter fibres to observe 150 spectra simultaneously covering two spectral ranges; the '*V*-band' data cover 3900–5600 Å and the '*R*-band' data cover 5400–7500 Å. When estimating redshifts, these two bands were spliced together to maximize the signal. However, to avoid problems with discontinuities and dispersion changes, only the *V*-band spectra were used to estimate velocity dispersions. The pixel scale was 1.64 Å and the average 1σ spectral resolution was $\sim$140 km s^{-1}.

Not all the $\sim$136 000 galaxy spectra of the full 6dFGS redshift survey are suitable for velocity dispersion measurements, and we applied a number of criteria in order to define the 6dFGSv sample. We only selected galaxies with the higher quality redshift flags, $Q = 3$–5, see Jones et al. (2004). This ensured that the selected spectra had reliable redshifts before their use for velocity dispersion information. At redshifts greater than 16 500 km s^{-1}, the important strong Mg*b* feature starts to be affected by the red wavelength cut-off of the 6dF *V*-band spectra; hence, we excluded galaxies with redshifts greater than 16 500 km s^{-1}. Further selection was made by spectral classification, based on the best-matching template spectra identified in the redshift estimation. This was initially based on the *R*-value returned from our cross-correlation analysis (see Section 2.2) which reflected how closely the galaxy spectrum matched that of our K-giant star templates. We found that spectra with an *R*-value of 8 had a velocity dispersion uncertainty of $\sim$0.12 dex. Hence, as a practical choice we used $R > 8$ criteria to select spectra that gave sufficiently reliable velocity dispersion measurements for our study. These various selection criteria restricted the total sample for velocity dispersion measurements to $\sim$18 000 galaxies.

While the above filtering process excluded spectra with strong emission lines, about $\sim$690 spectra had weak emission features. All spectra were visually checked, and poorly subtracted sky lines, foreground Hβ emission lines and weak galaxy emission lines (e.g. Hβ, [OIII] 4959/5007) were removed by local interpolation. We tested the sensitivity of our interpolation procedure by running an alternative pixel-based analysis in which the pixels that were previously modified by the interpolation were flagged as invalid. The derived velocity dispersions changed, on average, by only 1 km s^{-1}; the rms scatter of the difference was 15 km s^{-1}. On average, the removal of the weak emission features by the local interpolation technique increased the *R*-value by 3 and changed the derived velocity dispersions by –7 km s^{-1} with an rms scatter of 17 km s^{-1}.

2.2 Velocity dispersion measurements

Our analysis of the 6dF *V*-band spectra was undertaken in IRAF using the RV package. The `fxcor` routine, which implements the method of Tonry & Davis (1979, hereafter TD79), was used for the velocity dispersion determination. Spectra of a set of template stars ranging

Table 1. 6dFGSv stellar templates used with `fxcor`.

Name	Type	Velocity ($km\,s^{-1}$)	Plate	Fibre	FWHM (Å)
HD 223679	G8 III	+4	2	62	5.672
HD 813	G8/K0 IV	+24	2	109	5.211
HD 225166	G8/K0 IV	+123	1	86	5.365
CD-45 15239	K0	+39	2	101	5.107
HD 214	K1 III	+63	1	130	5.459
HD 224420	K1 III	+66	1	116	5.212
HD 321	K2 III	+39	2	137	5.154

in stellar type from G8 to K2 giants were observed with 6dF for the analysis (see Table 1).

To prepare for cross-correlation, the spectra were shifted to a rest-frame wavelength based on the redshift calculated in `runz` (Colless et al. 2001; Saunders, Cannon & Sutherland 2004) and rebinned to a log-wavelength scale. Spectra were truncated to have a minimum wavelength of 4000 Å, and a maximum limit depending upon the redshift of the galaxy; this ranged from 5570 Å at $z = 0$ to 5280 Å at $z = 0.055$. Cropping the spectra in this way gave the maximal coverage of desired spectral features such as Mg and Fe lines, while excluding problematic features such as the night sky line residuals of [O I] 5577 and intrinsically broad Ca H&K spectral lines. The spectral continuum was then subtracted, and 5 per cent of the pixels at each end of the spectra were apodized to prevent ringing in the correlation. The spectra were zero-padded and converted to Fourier space, and then filtered with a ramp filter to remove any high-frequency noise or low-frequency power due to continuum residuals and the apodization.

The galaxy spectra were correlated with the templates, and the largest peak in Fourier space was fitted over a range of 11 pixels using a Gaussian function to determine the centre and full width at half-maximum (FWHM). The FWHM was converted to an estimated galaxy velocity dispersion using the empirically established response, for each template, of the cross-correlation peak to velocity broadening. The final velocity dispersion was the average of all templates, weighted by the strength of the cross-correlation, R.

As an independent test of our velocity dispersion measurement procedure we used the spectra from the MILES library (Sánchez-Blázquez et al. 2006) which have an FWHM spectral resolution of 2.54 Å, i.e. a factor of 2 lower than the 6dF data set. We selected six stars with spectral types ranging from G8III to K1III. These were broadened to a range of velocity dispersions, degraded to a range of S/Ns and matched to the spectral range and resolution characteristics of the 6dF data set. For each input velocity dispersion and S/N, we produced a set of ∼1000 mock spectra and these were processed with our pipeline using the templates listed in Table 1. The systematic differences between the input velocity dispersions and those recovered are presented in Fig. 1. The systematic biases are typically less than 0.02 dex. At lowest S/N, the biases increase to 0.04 dex. Our `fxcor`-based pipeline best recovers the input velocity dispersions from the spectra constructed from the two K0III stars as this is the average spectral type of our templates.

The 6dF instrument, like many earlier multi-fibre spectrograph systems (e.g. WYFFOS; see Moore et al. 2002), has an instrumental profile that varies non-linearly both along the spectrum from a single fibre and from fibre to fibre (see Fig. 2). Also, over the six years of the 6dF survey, the resolution showed variations due to causes such as spectrograph focus and fibre degradation. The average 6dF spectral resolution was 140 $km\,s^{-1}$ with 95 per cent of fibres having mid-

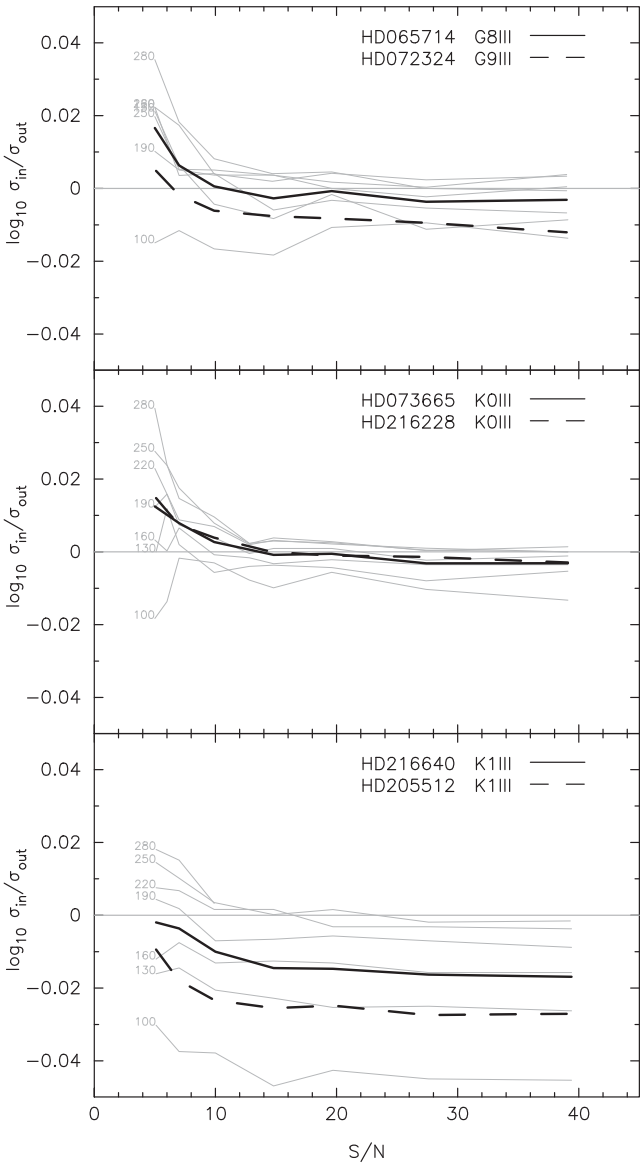

Figure 1. Our `fxcor`-based pipeline systematics. The log ratio of the input and the recovered velocity dispersions is plotted against S/N. The input velocity dispersions tested were 100, 130, 160, 190, 220, 250 and 280 $km\,s^{-1}$. The black lines are the average values. The grey lines show the individual velocity dispersions; for clarity, these are only plotted for the first star listed in each panel.

wavelength resolutions between 128 and 150 $km\,s^{-1}$. Hence there were, in some cases, significant differences in resolution between the template and object spectra. It is implicit in the TD79 method that the instrumental resolution of the template spectrum and that of the galaxy spectrum are identical, so that

$$\mu^2 = \sigma^2 + 2\tau^2, \quad (1)$$

where μ is the width of the cross-correlation peak, τ is the dispersion due to instrumental resolution and σ is the dispersion due to velocity broadening. The fact that this was not always the case would therefore result, unless corrected, in biased velocity dispersion estimates.

Any difference in resolution between template and object spectra ($\Delta\tau$) is simply added in quadrature to the cross-correlation peak width. However, prior to the cross-correlation the spectra are filtered

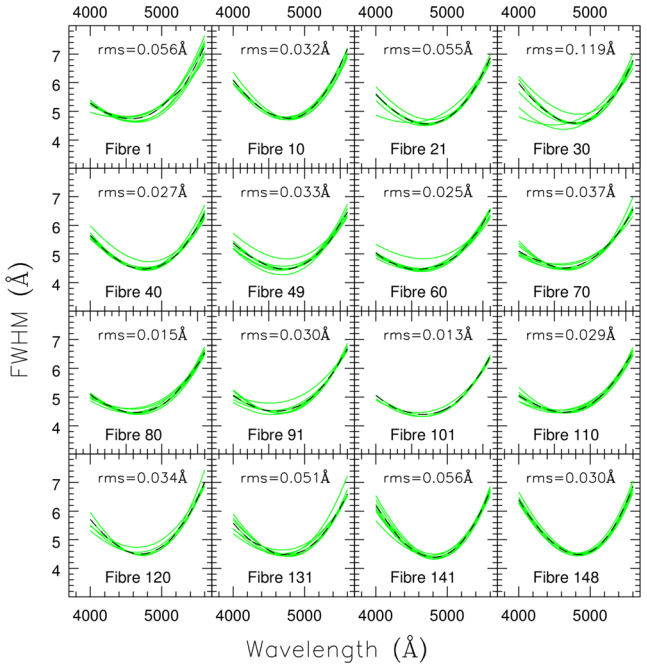

Figure 2. Instrumental spectral FWHM of *V*-band spectra for a subset of 6dF fibres. The instrumental FWHM were measured from multiple HgCdHe arc spectra observations and fitted with a third-order polynomial. The dashed line shows the median resolution as a function of wavelength. A FWHM of 5 Å corresponds to a 1σ resolution of 127 km s^{-1}.

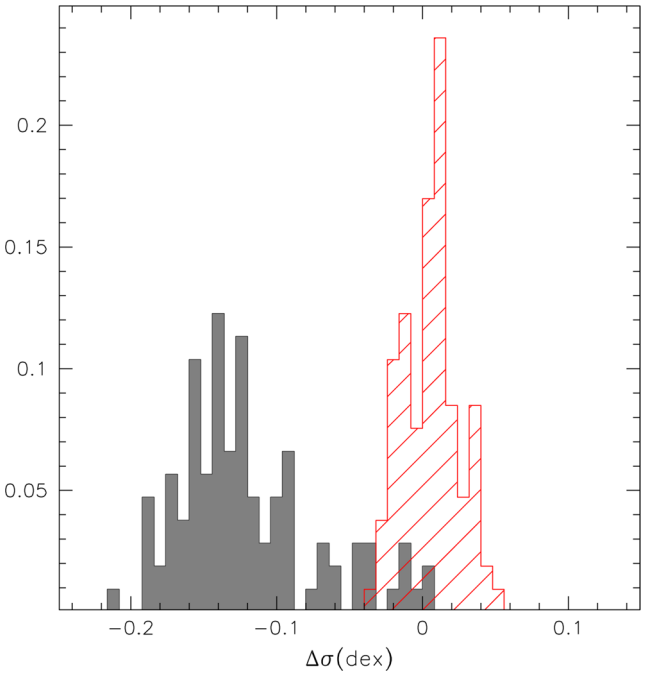

Figure 3. Skyflat velocity dispersions for 6dF fibre #4 before and after applying a resolution correction. The distributions of the differences between skyflat velocity dispersions before (the shaded histogram) and after (the hatched histogram) applying a resolution correction for the case of an applied broadening of 150 km s^{-1} and a template with a spectral resolution of 166 km s^{-1}. This is the case with the poorest resolution and hence the largest correction.

and, as seen in fig. 1 of TD79, this changes the relationship between the width of lines in the spectra, τ, and the width of the peak, μ. To properly correct for differences in resolution, we measured the change in μ as a function of $\Delta\tau$. Autocorrelation of a stellar template was performed over a range of τ values equivalent to adding in quadrature template and object spectra with differences in resolution of between -40 and $+40$ km s^{-1}. The μ values responded in a linear fashion to changes in τ, and were essentially independent of the stellar template and the wavelength range of the spectra. Based on these results, a look-up table was generated giving the fits as a function of $\Delta\tau$, from which a corrected cross-correlation peak width μ could be obtained. A zeroth-order estimation of the resolution of the template and object spectra, centred roughly around 5200 Å (the major source of signal in the Fourier cross-correlation comes from the Mg and Fe lines in early-type galaxies), gave $\Delta\tau$ for each observation, and the corresponding μ was then converted to a resolution-corrected velocity dispersion using the normal template calibration curve.

Twilight exposures (skyflats), which result in high S/N solar spectra being observed in each fibre, provided a useful test of our resolution correction procedure. The source spectrum is identical in each fibre, but the different fibres and positions on the camera mean the resolution naturally varies. We selected three fibre spectra with spectral resolutions of 126, 140 and 166 km s^{-1} to act as the spectral templates. All the twilight spectra were then broadened by 100, 150 and 200 km s^{-1} to simulate the galaxy observations. We then applied our resolution correction procedure and confirmed that the input broadening was recovered. Fig. 3 shows the results of using the 166 km s^{-1} resolution fibre as the template with the twilight sky spectra broadened by 150 km s^{-1}, and demonstrates the validity of our procedure.

As a further independent test of our resolution correction, we examined 120 galaxies that also had velocity dispersion measurements from the Sloan Digital Sky Survey (SDSS). We divided these galaxies into subsamples with lower and higher 6dF resolution ($\tau <$ 135 km s^{-1} and $\tau >$ 145 km s^{-1}). The comparison confirmed the existence of the resolution bias and validated the correction procedure. It also demonstrated that the correction introduced no appreciable increase in scatter ($\leq$10 km s^{-1}).

Consequently, the resolution correction using this method was applied to all the 6dFGS velocity dispersion measurements. Fig. 4 shows the scale of these corrections, as a function of the difference in resolution between template and object spectra ($\Delta\tau$), for the velocity dispersion sample. The figure clearly illustrates how the correction had a much more significant impact for lower velocity dispersion measurements. Moreover, the correction is simple, well behaved at all velocity dispersions, and straightforward, supporting the adoption of the correction procedure.

While many previous FP peculiar velocity surveys have used the cross-correlation technique as implemented in `fxcor` to measure velocity dispersions, e.g. the ENEAR survey (Wegner et al. 2003) and the NOAO Fundamental Plane Survey (NFPS; Smith et al. 2004), recent studies of galaxy dynamics have mainly used pixel-based fitting techniques. In order to directly assess the difference between these two widely used techniques, we have measured velocity dispersions with PPXF (Cappellari & Emsellem 2004) for a subset of our spectra. We selected the four highest resolution templates (HD 813, CD-45 15239, HD 224420, HD 321) and the galaxy spectra that were observed with instrumental resolutions that were greater than that of the four templates. Extra instrumental (Gaussian) broadening was added to the templates to match the individual resolutions of the galaxy spectra, and the velocity dispersions were determined using PPXF. There is good agreement between the two techniques with

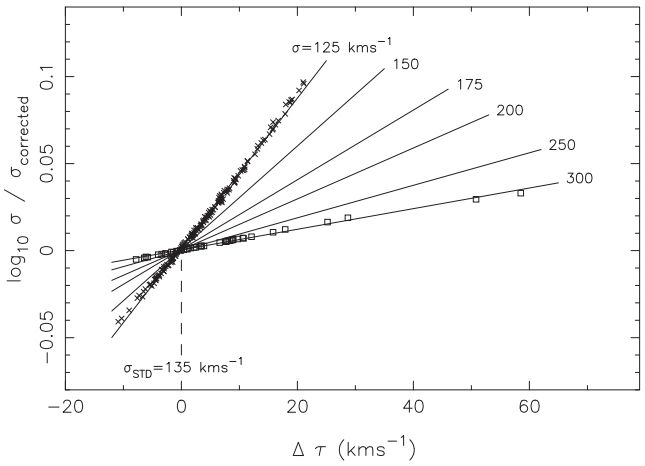

Figure 4. The scale of these corrections, as a function of the difference in resolution between template and object spectra ($\Delta\tau$), for the velocity dispersion sample. The lines show the average correction applied for objects with a σ of 125, 150, 175, 200, 250 and 300 km s^{-1}. For clarity, the actual corrections applied are only shown for individual galaxies with $\sigma \sim 125$ km s^{-1} (crosses) and $\sigma \sim 300$ km s^{-1} (squares).

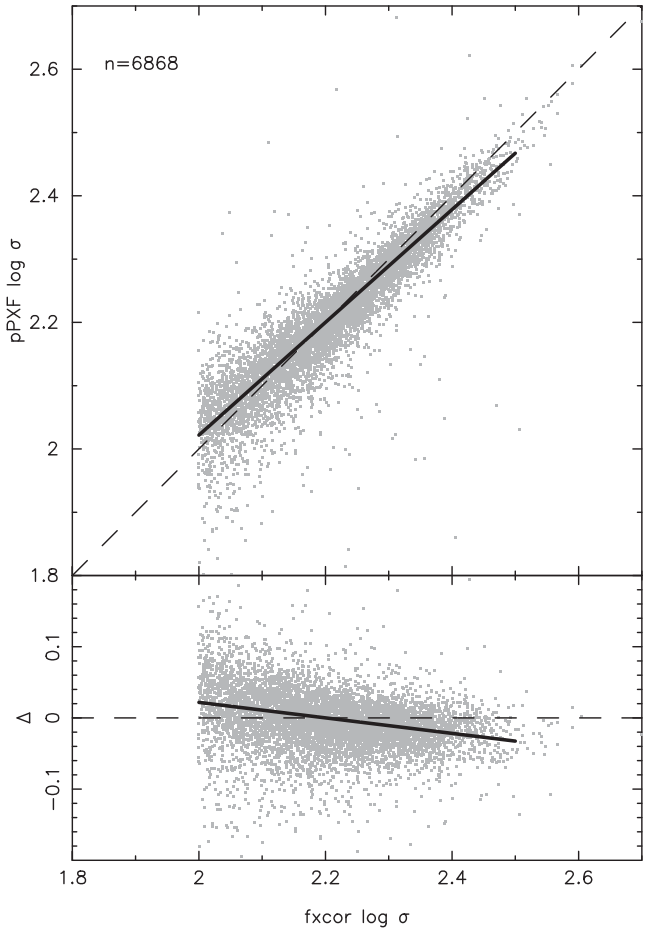

Figure 5. Comparison of `fxcor`- and PPXF-based velocity dispersion measurements. The solid line indicates the best-fitting linear relation between the two sets of measurements. This has the form: $\log\sigma(\mathrm{pPXF}) = 0.891 \times \log\sigma(\mathrm{fxcor}) + 0.239$.

only a moderate systematic difference (see Fig. 5). The observed systematic offsets at velocity dispersions of 2.00 and 2.50 dex are relatively small, i.e. +0.022 and −0.032 dex, respectively. These differences between the methods are comparable to the systematic variations that can result from template mismatch (see Fig. 1). We conclude that both `fxcor` and PPXF are limited by systematic uncertainties from template mismatch and spectral filtering to a precision of about 0.02 dex. As shown below, this is substantially less than the typical random error for the 6dFGS velocity dispersions.

We note that any systematic trend in velocity dispersion measurements will influence the derived parameters of the FP, notably the coefficient associated with the $\log\sigma$ term. Clearly, this is a potential source of bias and is particularly relevant when combining data sets from different sources. Fortunately, there is now a large number of early-type galaxies with velocity dispersion measurements from more than one source (see Section 2.5) which allow this bias to be fully investigated.

2.3 Velocity dispersion uncertainties

Measurement errors in velocity dispersions are due to a number of factors: template–galaxy mismatch, noise in the spectra, non-optimal filtering and calibration errors. Errors due to template mismatch were minimized by using appropriate templates, which in the case of early-type galaxies means late G-type and early K-type stars. Filter values were optimized using a range of stellar templates. Calibration errors depend upon the accuracy of the function used to fit the template calibration curve, in this case a fifth-order polynomial. Twilight flats were used to test the scale of calibration errors, and these were found to be negligible, as they did not exceed 0.005 dex for velocity dispersions larger than ∼100 km s^{-1}.

The statistical uncertainties of our velocity dispersion measurements were determined via a bootstrap technique. Along with the galaxy spectrum, the 6dF data reduction pipeline also provides an associated variance spectrum. We used the galaxy and variance spectra to create many (∼900) bootstrap realisations of the original spectrum, and for each we measured the velocity dispersion. We adopted the standard deviation of these measurements as the statistical error of the velocity dispersion. This procedure was tested by using synthetic spectra that mimicked the characteristics of the 6dF spectra, i.e. spectral coverage, velocity dispersion and S/N range, and was found to give reliable estimates of the measurement errors. For the lowest S/N spectra modelled, i.e. S/N = 5, this technique returns values for the errors that are corrected, on average, at the level of a few (∼5) per cent. Fig. 6 illustrates how the fraction error depends on the inverse S/N.

2.4 The 6dFGSv velocity dispersion catalogue

To construct our final 6dFGSv velocity dispersion sample, several criteria were applied. As previously noted, we excluded galaxies with $z > 0.055$, where the strong Mg*b* feature is affected by the red limit of the *V*-band spectral coverage. In order to ensure a reliable set of measurements, we only included galaxies that had spectral measurements with S/N > 5, $R > 8$ and $\sigma > 100$ km s^{-1}. These criteria resulted in a velocity dispersion sample with 11 520 measurements; 185 galaxies have two measurements and 10 have three measurements.

The 6dFGSv velocity dispersion catalogue is presented in Table 2 for an example set of galaxies; the velocity dispersion values given in this table are not aperture corrected. The full sample has a median

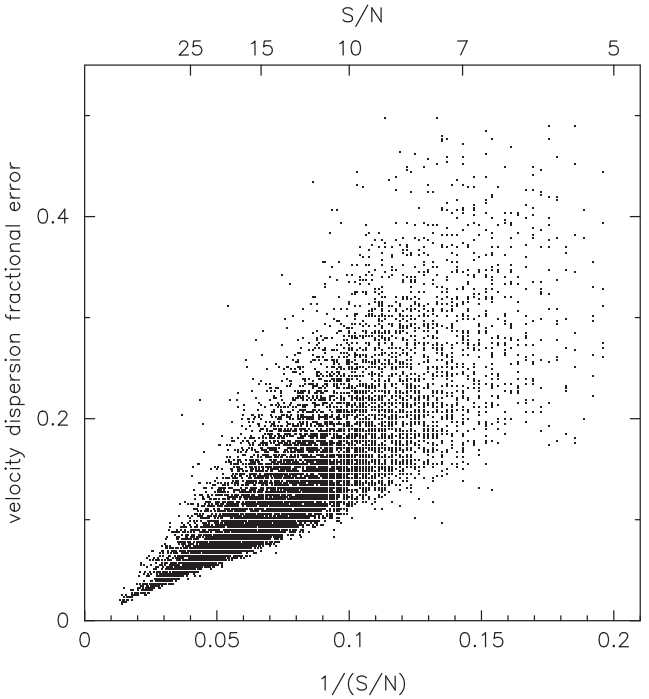

Figure 6. Velocity dispersion fractional error as a function of inverse S/N. 0.8, 4.7 and 19.8 per cent of the 6dFGSv sample have fractional errors greater than 0.4, 0.3 and 0.2, respectively.

velocity dispersion of 163 km s^{-1}, a median S/N of 12.9 Å^{-1} and a median velocity dispersion error of 12.9 per cent.

2.5 External comparisons

There are a sizeable number of galaxies in the 6dFGSv sample that have dispersion velocity measurements from previous large studies, i.e. the Streaming Motions of Abell Clusters (SMAC) survey (Hudson et al. 2001); the ENEAR redshift-distance survey (Wegner et al. 2003); the NFPS (Smith et al. 2004) and the SDSS DR8 (Aihara et al. 2011). The comparison of the 6dFGSv velocity dispersions with those values reported by SDSS and NFPS is presented in Fig. 7. The best-fitting relation between these independent measurements was calculated by minimizing the χ^2 sum

$$(a\,\sigma_x + b - \sigma_y)^2/(\epsilon(\sigma_x)^2 + \epsilon(\sigma_y)^2), \quad (2)$$

where σ_x and $\epsilon(\sigma_x)$ refer to the 6dFGSv measurements and their errors, and σ_y and $\epsilon(\sigma_y)$ refer to the external data set. Data points with $\chi^2 > 6$ were excluded from the fit. In Table 3, we summarize the observed relations between 6dFGSv velocity dispersions and those from the four external sources. All comparisons are consistent with unit slope, and hence, within the typical slope uncertainty of 0.035 dex, there is no evidence of systematic bias. Also listed in Table 3 are the median offsets between the velocity dispersion measurements of these four external sources and 6dFGSv. While the only significant offset is that for the 6dFGSv–ENEAR comparison, i.e. $\Delta \log \sigma = 0.021 \pm 0.005$, this difference is similar in size to that found when intercomparing σ data sets (see Hudson et al. 2001, table 2). A detailed intercomparison of the various velocity dispersion data sets, including the four considered here, will be presented in future work where a standardized all-sky velocity dispersion catalogue optimized for FP studies will be constructed.

3 PHOTOMETRIC MEASUREMENTS

3.1 PSF-corrected effective radii and surface brightnesses

The FP is the relationship between two photometric parameters, a characteristic radius and the mean surface brightness within that radius, and the central velocity dispersion. The key step in determining a galaxy's photometric parameters is the measurement of the total flux. Early work (e.g. Burstein et al. 1987) derived the total magnitude m_T through an $r^{1/4}$ growth curve fitted to photoelectric aperture photometry, and measured the effective (half-light) radius R_e by interpolation. The mean surface brightness $\langle\mu_e\rangle$ within R_e was determined via

$$\langle\mu_e\rangle = m_T + 2.5\log(2\pi R_e^2). \quad (3)$$

Table 2. 6dFGSv velocity dispersion catalogue. The columns are as follows: (1) 6dFGSv unique reference number; (2) 6dFGS input catalogue standard galaxy name; (3) 2MASS Extended Source Catalogue designation; (4) observation Modified Julian Date; (5) heliocentric redshift; (6) signal-to-noise ratio per Å measured from a region between 4900 and 5000 Å; (7) TD79 *R*-value in the Fourier cross-correlation; (8) velocity dispersion in km s^{-1} (6.7 arcsec diameter fibre aperture) corrected for instrumental resolution but not corrected for aperture size; (9) log error in the velocity dispersion, i.e. $\epsilon_{\log\sigma} \equiv \delta\log\sigma$. The full version of this table has 11 315 galaxies (185 galaxies have two measurements, 10 have three measurements; all are listed, so this table has 11 520 data lines) and is provided in the online Supporting Information.

# (1)	6dFGS ID (2)	2MASS XSC name (3)	MJD (4)	z_{helio} (5)	S/N (6)	TDR (7)	σ (8)	$\epsilon_{\log\sigma}$ (9)
00001	g0000144-765225	2MASXJ00001440−7652248	53614.60	0.0533	13.2	14.0	129.0	0.073
00002	g0000222-013746	2MASXJ00002213−0137463	52962.44	0.0383	24.1	18.4	199.1	0.023
00003	g0000235-065610	2MASXJ00002348−0656103	52966.46	0.0376	15.2	16.6	156.2	0.045
00004	g0000251-260240	2MASXJ00002509−2602401	52846.78	0.0508	13.2	13.0	218.5	0.040
00005	g0000356-014547	2MASXJ00003564−0145472	52962.44	0.0244	14.0	16.3	133.4	0.066
00006	g0000358-403432	2MASXJ00003574−4034323	52881.58	0.0500	9.6	8.9	143.7	0.093
00007	g0000428-721715	2MASXJ00004283−7217148	53618.50	0.0348	13.9	19.0	151.2	0.049
00008	g0000459-815803	2MASXJ00004596−8158024	53646.46	0.0422	14.9	9.6	200.9	0.058
00009	g0000482-551119	2MASXJ00004816−5511192	52969.51	0.0323	11.1	14.4	135.4	0.081
00010	g0000523-355037	2MASXJ00005234−3550370	52872.63	0.0520	14.9	10.2	242.3	0.048
00011	g0000532-355911	2MASXJ00005317−3559104	52872.63	0.0500	15.6	13.3	207.0	0.040
00012	g0000558-255421	2MASXJ00005579−2554210	52846.78	0.0505	10.3	15.4	188.4	0.042
00012	g0000558-255421	2MASXJ00005579−2554210	52880.53	0.0505	15.6	19.5	149.9	0.038

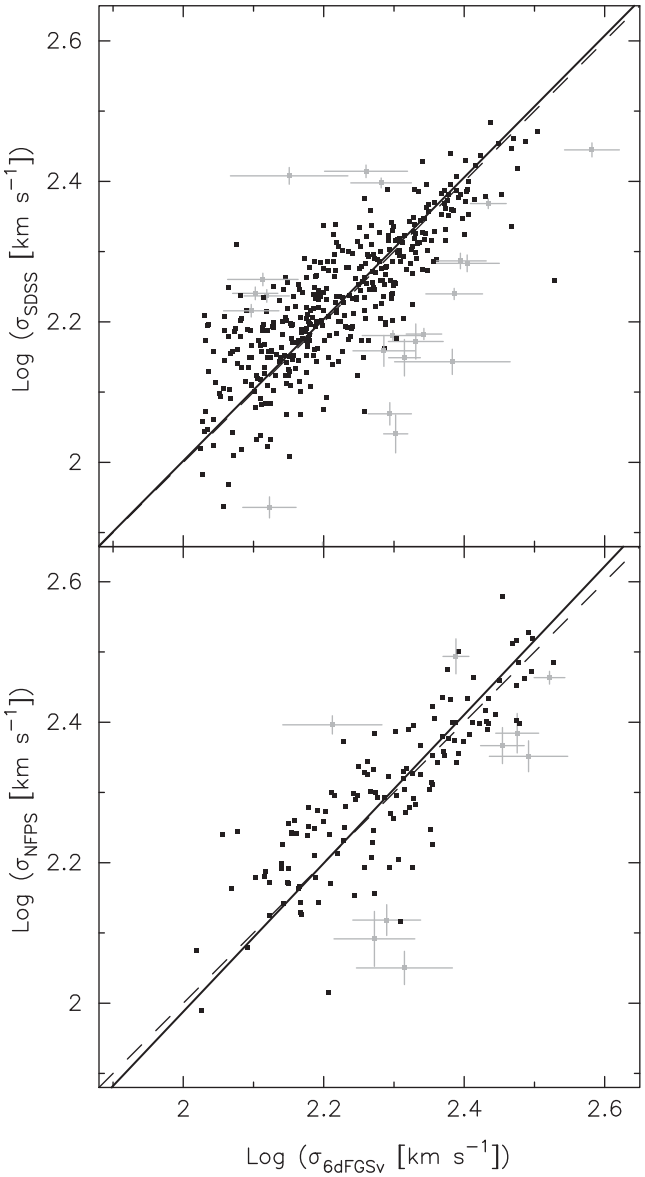

Figure 7. Comparisons of 6dFGSv velocity dispersion measurements with those from SDSS (top panel) and NFPS (lower panel). The dashed line shows the one-to-one relationship for reference. The solid line shows the best linear fit, calculated as described in Section 2.5. The black squares show galaxies included in the fit. The grey squares show objects that were excluded from the fit. For clarity, only error bars on the excluded data points are displayed.

For simplicity, early FP studies using CCD imaging data mimicked this approach (e.g. Lucey & Carter 1988; Lucey et al. 1991) with the addition of an empirical correction for the PSF blurring. Later work using CCD imaging data undertook more sophisticated analysis to determine the total magnitude. For example, Jorgensen, Franx & Kjaergaard (1995a) fitted ellipses to the surface photometry and used model fitting ($r^{1/4}$) of the growth curves of the photometry. Bernardi et al. (2003) used the $r^{1/4}$ (or exponential) 'model' magnitudes from the SDSS image processing software which are derived from PSF-convolved two-dimensional surface fitting. Alternative approaches used to determine R_e include fitting seeing-convolved Sérsic models to circularized profiles or major and minor axis profiles (Saglia et al. 1997; D'Onofrio et al. 2008) or full two-dimensional surface brightness fitting of a Sérsic model convolved with a PSF (Gargiulo et al. 2009) or Sérsic plus exponential disc models (e.g. Fernández Lorenzo et al. 2011).

For the 6dFGSv sample, we analysed the imaging data from the 2MASS survey (Skrutskie et al. 1997) to derive the FP photometric parameters. The key advantage of the 2MASS data is the near-complete all-sky coverage and the excellent photometric uniformity. Furthermore, the online NASA/IPAC Infrared Science Archive provides straightforward access to the 2MASS image tiles, which allows the measurement of additional photometric parameters not provided by the 2MASS Extended Source Catalog (XSC; Jarrett et al. 2000).

The 2MASS PSF has a relatively large FWHM (∼3.2 arcsec) and required the development of a procedure to derive PSF-corrected photometric parameters. For each target galaxy, we analysed the pixel data provided by the 2MASS Extended Source Image Server as follows. The 2MASS image data for the *J*, *H* and *K* bands were analysed independently. We adopted the total apparent magnitude (m_T) reported by 2MASS from the 'fit extrapolation' method (i.e. `j_m_ext`, `h_m_ext`, `k_m_ext`; see Jarrett 2000). First we determined the circular apparent effective radius (r_{app}) of the target galaxy on the 2MASS image by finding, via interpolation, the radius that contained half the total flux. A model two-dimensional Gaussian PSF image was derived from stars on the parent 2MASS data tile. GALFIT (Peng et al. 2010) was used with the galaxy image and model PSF image as inputs to find the best-fitting two-dimensional Sérsic model. The half-light radius was determined for the Sérsic model before and after convolution with the PSF (r_{model} and r_{smodel}, respectively) to find the PSF correction (Δr) given by

$$\Delta r = r_{smodel} - r_{model}. \quad (4)$$

The PSF-corrected effective radius (R_e) was then derived via

$$R_e = r_{app} - \Delta r. \quad (5)$$

Table 3. Comparison of 6dFGSv velocity dispersion measurements with external sources. For this comparison, aperture corrections to the velocity dispersions have been applied, see Section 5.1. n is the number of objects common between the data set and 6dFGSv. n_{FIT} is the number of objects remaining after the $\chi^2 > 6$ clipping has been applied. a and b are defined in equation (2). $\Delta \log \sigma$ is the median offset (6dF – Source) between the two systems after clipping. rms is the scatter of the difference between the two systems after clipping.

Source	n	n_{FIT}	a	b	$\Delta \log \sigma$	rms	χ^2
SDSS	419	397	1.009 ± 0.025	-0.016 ± 0.057	0.008 ± 0.004	0.057	0.984
NPFS	146	137	1.056 ± 0.045	-0.126 ± 0.107	0.010 ± 0.006	0.058	1.060
SMAC	99	93	0.931 ± 0.035	$+0.167 \pm 0.081$	0.005 ± 0.006	0.045	1.003
ENEAR	174	155	0.985 ± 0.030	$+0.057 \pm 0.068$	0.021 ± 0.005	0.049	1.351

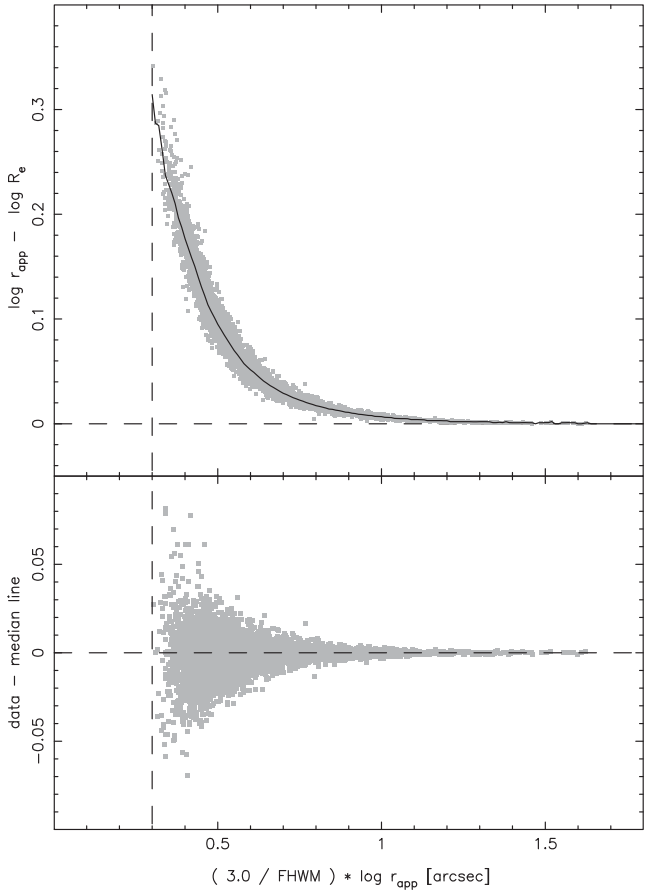

Figure 8. *J*-band PSF correction as determined by GALFIT modelling. The upper panel displays the measured PSF correction as a function of r_{app} normalized by the PSF FWHM on the parent 2MASS data tile. The vertical dashed line is where $r_{app} = 2$ arcsec. The black line in the upper panel follows the median values. For values of (3.0/FWHM) log r_{app} of 0.3, 0.4, . . . , 1.4, the log r_{app}–log R_e corrections are 0.3143, 0.1768, 0.0950, 0.0515, 0.0291, 0.0173, 0.0108, 0.0068, 0.0040, 0.0028, 0.0020, 0.0010, respectively. The lower panel displays the residual between a median trend and the data.

Hence, the effective radius is determined as the empirical half-light radius corrected for the effects of the PSF using the Sérsic model fit. Note that the GALFIT model fit is only used to determine the PSF correction. The size and variation of Δr as a function of r_{app} for the *J* band are given in Fig. 8.

For *J*-band apparent effective radii of 10, 8, 6, 4, 3 and 2 arcsec, the average Δr and its dispersion are (0.15, 0.04), (0.20, 0.04), (0.27, 0.05), (0.51, 0.12), (0.88, 0.21) and (1.87, 1.10), respectively. As the 2MASS PSF is nearly Gaussian, these corrections are very similar to those derived from smoothing a Sérsic model with the appropriate 2D Gaussian. For galaxies with apparent effective radii of 2 arcsec, the PSF correction is of similar size and so the relative uncertainty of the correction is near unity. Hence, this is the practical limit where galaxy sizes can be measured reliably on the 2MASS image tiles. Only 2 per cent of the 6dFGSv FP sample have apparent effective radii less than 2.4 arcsec, where the average correction is 1.4 arcsec and hence the 2MASS image data are suitable for our study.

The derived PSF-corrected *JHK* effective radii for 11 102 galaxies are presented in Table 4. For 213 galaxies listed in Table 2, i.e. 1.9 per cent of the sample, derivation of reliable photometric parameters was not possible due to either deblending/masking issues or because r_{app} was less than 2 arcsec.

The comparison of the PSF-corrected effective radii derived independently from the *J*- and *K*-band 2MASS image data is presented in Fig. 9. There is very good agreement between the two sets of measurements. On average, the measured *J*-band radii are ∼7 per cent larger than those in the *K* band. If the errors are equally distributed between the two data sets, the average error on each measurement is 12 per cent.

For each galaxy, the PSF-corrected effective surface brightness $\langle\mu_e\rangle'$ is computed as

$$\langle\mu_e\rangle' = m_T + 2.5\log(2\pi R_e^2), \quad (6)$$

where m_T is the 2MASS total magnitude (e.g. `j_m_ext`) and R_e is the PSF-corrected effective radius. In Section 5.2, we describe corrections applied to $\langle\mu_e\rangle'$ for cosmological surface brightness dimming, the *k*-correction and galactic extinction in order to derive the fully corrected effective surface brightness $\langle\mu_e\rangle$.

3.2 Internal X_{FP} comparisons

As is well known the measurements of R_e and $\langle\mu_e\rangle$ are highly correlated; if R_e is overestimated, then a fainter $\langle\mu_e\rangle$ is derived, and conversely (e.g. Burstein et al. 1987; Lucey et al. 1991). However, the linear combination of these parameters that appears in the FP, which is approximately $X_{FP} \equiv R_e - 0.3\langle\mu_e\rangle$, is well determined (e.g. Jorgensen et al. 1995a). In Fig. 10, we compare our X_{FP} measurements for the *J* and *K* bands. To aid the comparison for each band, the average effective surface brightness has been subtracted from the $\langle\mu_e\rangle$ values which ensures that the average ΔX_{FP} is near zero. The low intrinsic scatter between these two independent measurements implies excellent internal precision for each data set (regardless of any intrinsic colour–size relation). The implied average measurement error of X_{FP}, if equally divided between the two data sets, is 0.013 dex (3 per cent).

Our analysis used the total apparent magnitude reported by 2MASS, e.g. `j_m_ext`, and PSF-corrected apparent effective radius derived using GALFIT. An alternative approach would have been to directly use the total Sérsic magnitude and effective radii returned by GALFIT. The X_{FP} parameters from these two techniques are in excellent agreement (see Fig. 11) with an average difference of 0.001 dex and the scatter in the difference of 0.021 dex. Hence, for the relatively low S/N 2MASS image data, these two techniques are equivalent. In our analysis, we prefer our approach as this does not force a particular parametric photometric form on the galaxy light distribution.

3.3 External X_{FP} comparisons

Pahre (1999) measured *K*-band FP photometric parameter for 341 nearby early-type galaxies primarily in clusters. We have analysed the 2MASS *K*-band image data following the procedure outlined above and measured R_e and $\langle\mu_e\rangle$ for the Pahre sample. 2MASS-based measurements could be derived for 229 galaxies; the missing galaxies are either too faint, unresolved at the 2MASS resolution or strongly contaminated by an adjacent star. The comparison of the X_{FP} measurements is presented in Fig. 12. There is excellent agreement between the two data sets with a systematic offset of 0.017 dex. The implied average measurement error, if equally divided between the two data set, is 0.014 dex (3 per cent).

The SMAC survey (Hudson et al. 2004 and references therein) presented FP photometric parameters derived from either *R*- or

Table 4. 6dFGSv 2MASS photometric parameters. The columns are as follows: (1) 2MASS XSC name; (2) *J*-band total extended magnitude (`j_m_ext`); (3) *J*-band PSF FWHM in arcsec; (4) *J*-band Δr correction applied in arcsec; (5) log *J*-band PSF-corrected circular effective radius in arcsec; the observed mean effective surface brightness can be derived via equation 6; (6) *J*-band Sérsic index from GALFIT; (7) *H*-band total extended magnitude (`h_m_ext`); (8) *H*-band PSF FWHM in arcsec; (9) *H*-band Δr correction applied in arcsec; (10) log *H*-band PSF-corrected circular effective radius in arcsec; (11) *K*-band total extended magnitude (`k_m_ext`); (12) *K*-band PSF FWHM in arcsec; (13) *K*-band Δr correction applied in arcsec; (14) log *K*-band PSF-corrected circular effective radius in arcsec. The apparent magnitudes (j_m_ext, h_m_ext and k_m_ext) are from the 2MASS XSC and are not corrected for galactic extinction. The full version of this table is provided in the online Supporting Information.

	J band					*H* band				*K* band			
2MASS name	`j_m_ext`	FWHM	Δr	log R_e	Sérsic n	`h_m_ext`	FWHM	Δr	log R_e	`k_m_ext`	FWHM	Δr	log R_e
(1)	(2)	(3)	(4)	(5)	(6)	(7)	(8)	(9)	(10)	(11)	(12)	(13)	(14)
2MASXJ00001440−7652248	13.177	2.97	0.36	0.605	5.43	12.490	2.97	0.51	0.503	12.206	2.98	0.64	0.401
2MASXJ00002213−0137463	12.625	3.08	0.85	0.312	4.52	11.896	3.06	0.95	0.278	11.741	3.13	0.95	0.201
2MASXJ00002348−0656103	12.595	2.90	0.33	0.638	6.00	11.857	2.88	0.30	0.665	11.869	2.94	0.63	0.428
2MASXJ00002509−2602401	12.495	2.98	0.38	0.538	3.59	11.781	2.95	0.42	0.505	11.553	2.89	0.54	0.477
2MASXJ00003564−0145472	12.242	3.10	0.23	0.800	3.24	11.605	3.03	0.24	0.770	11.281	3.09	0.25	0.804
2MASXJ00003574−4034323	13.443	3.03	0.45	0.493	2.22	12.849	2.92	0.57	0.426	12.442	2.99	0.49	0.436
2MASXJ00004283−7217148	12.942	2.94	0.40	0.544	3.89	12.187	2.97	0.40	0.559	11.898	3.08	0.46	0.600
2MASXJ00004596−8158024	12.958	2.88	0.59	0.446	3.43	12.276	2.89	0.48	0.381	11.809	2.95	0.60	0.407
2MASXJ00004816−5511192	13.018	3.09	0.34	0.660	0.82	12.218	3.02	0.35	0.690	11.869	3.01	0.28	0.739
2MASXJ00005234−3550370	12.127	3.06	0.24	0.832	5.38	11.490	2.85	0.22	0.770	11.134	2.91	0.25	0.821
2MASXJ00005317−3559104	12.445	3.02	0.33	0.671	4.14	11.620	2.94	0.25	0.743	11.488	2.98	0.37	0.651

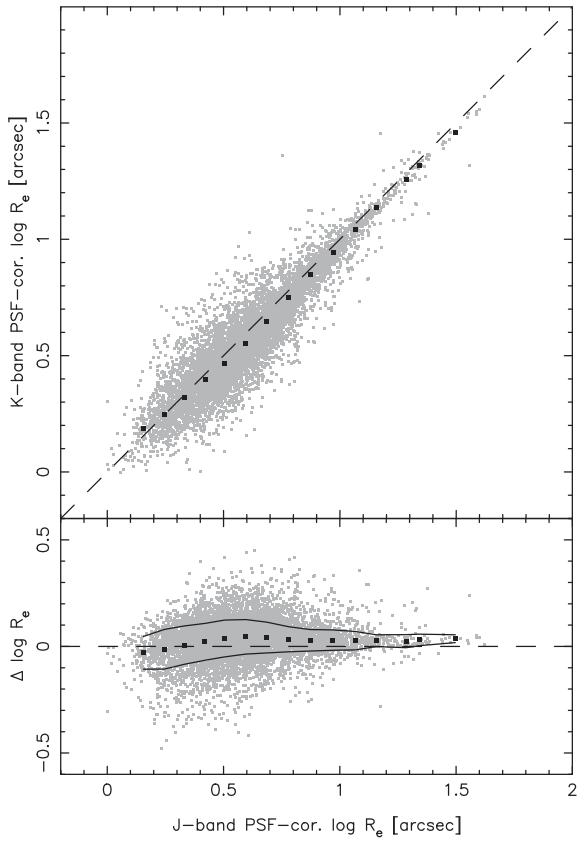

Figure 9. Comparison of the PSF-corrected *J*- and *K*-band measured R_e. The rms scatter of the difference is 0.078 dex. The squares are the median values at evenly log R_e steps. In the lower panel, the lines show the locations of ± one standard deviation in the distribution.

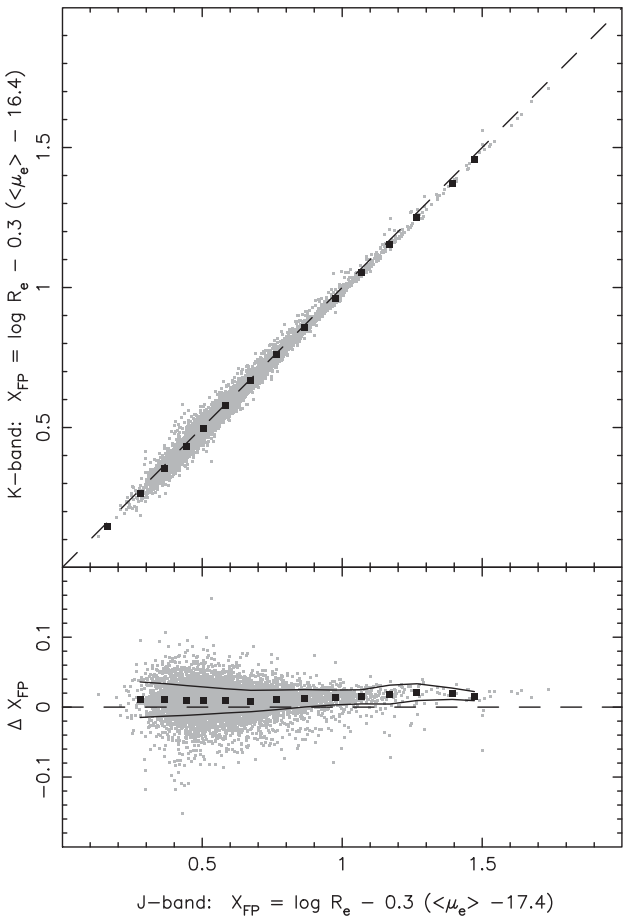

Figure 10. Comparison of X_{FP} ($\equiv \log R_e - 0.3\langle\mu_e\rangle$) for the *J*- and *K*-band measurements. The average effective surface brightness for the sample in each band has been subtracted from the $\langle\mu_e\rangle$ values. For this comparison, we include corrections to the effective surface brightnesses for galactic extinction, the *k*-correction and cosmological surface brightness dimming (see Section 5.2). The squares are the median values at uniform X_{FP} steps. In the lower panel, the lines show the locations of ± one standard deviation in the distribution. The rms scatter of the difference is 0.018 dex.

V-band data an all-sky sample of 699 early-type galaxies in 56 clusters. For all galaxies in the SMAC standardized FP catalogue (Hudso et al. 2001, table 7), we have analysed the 2MASS *J*-band image data following the procedure outlined above and measured R_e and $\langle\mu_e\rangle$. 2MASS-based measurements could be derived for 668

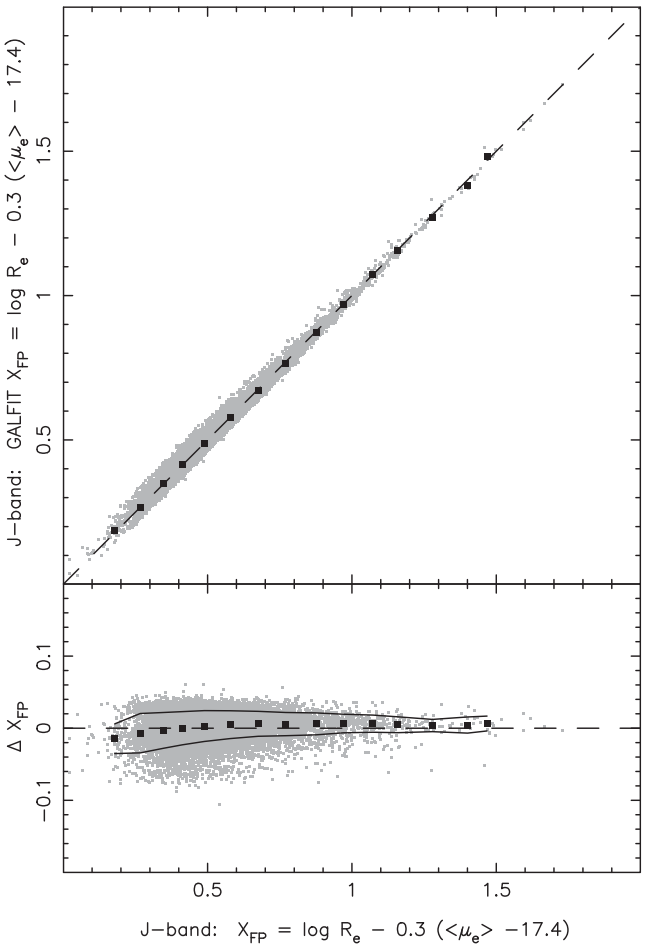

Figure 11. Comparison of X_{FP} derived from our technique and directly with GALFIT. To aid the comparison, the average effective surface brightness for the sample in each band has been subtracted from $\langle\mu_e\rangle$. The squares are the median values at uniform X_{FP} steps. In the lower panel, the lines show the locations of ± one standard deviation in the distribution. The rms scatter of the difference is 0.021 dex.

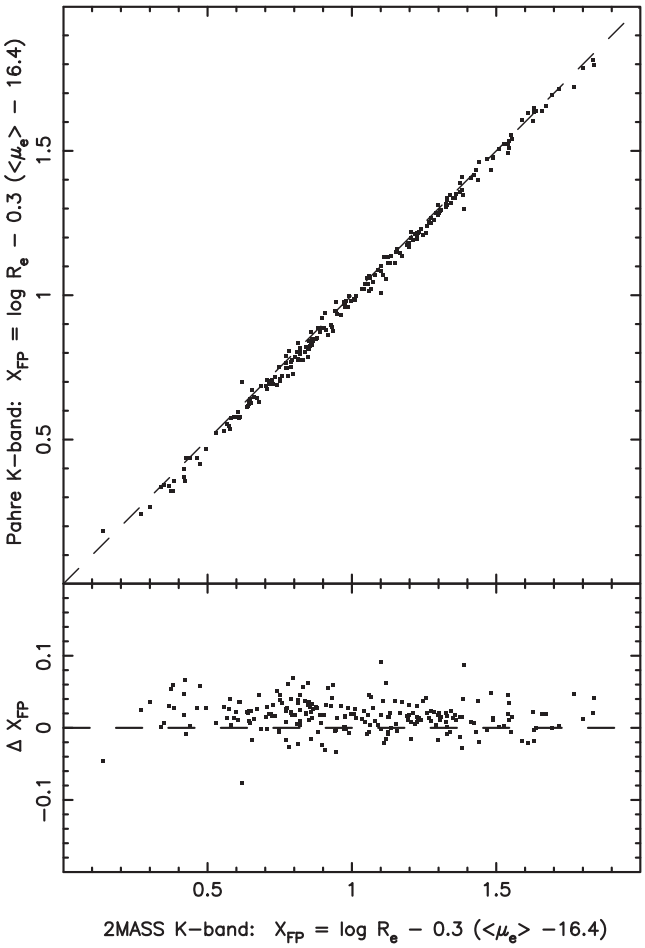

Figure 12. Comparison of the *K*-band X_{FP} for our 2MASS-based measurements and the Pahre measurements. The observed median offset (2MASS-Pahre) is 0.017 dex (equivalent to a magnitude offset of 0.05) and the rms scatter is 0.020 dex.

galaxies. On average $R_e^J / R_e^{V,R} = 0.70$. The comparison of the X_{FP} measurements is presented in Fig. 13. In this comparison, the average effective surface brightness in each band has been subtracted from the $\langle\mu_e\rangle$ values. The low intrinsic scatter between these two fully independent sets of measurements implies excellent internal precision for each data set. The implied average measurement error of X_{FP} for each band is 0.019 dex (4 per cent). The residual trend in the lower panel is a direct result of the colour–magnitude relation; at fixed $\log R_e(J)/R_e(R)$, $\Delta X_{FP} \propto \langle\mu_e(J)\rangle - \langle\mu_e(R)\rangle \propto J - R$ colour and $X_{FP} \propto J$ magnitude.

The ENEAR survey (da Costa et al. 2000) presented *R*-band FP photometric parameters for an all-sky sample of 1332 early-type galaxies. For all galaxies listed in the ENEAR photometric catalogue (Alonso et al. 2003), we have analysed the 2MASS *J*-band image data following the procedure outlined above and measured R_e and $\langle\mu_e\rangle$. 2MASS-based measurements could be derived for 1270 galaxies. The comparison of the X_{FP} measurements is presented in Fig. 14. There is good agreement between the two data sets, with an implied average measurement error of X_{FP} for each band of 0.033 dex (7.5 per cent).

In Magoulas et al. (2012, see section 3.3), we describe in detail how the uncertainties in R_e and $\langle\mu_e\rangle$ (and their correlated nature) are taken into account when we apply our maximum likelihood method to model the 3D FP.

4 VISUAL CLASSIFICATION

4.1 Overview

All galaxies in the 6dFGSv sample were examined visually to verify that they were bulge-dominated systems, appropriate for the FP analysis. Moreover, we attempted to roughly classify the types of galaxies in the sample by Hubble type, as well as to identify cases which were problematic either in type or in measurement. Visual classification was undertaken via a private purpose-built interface to the publicly accessible 6dFGS online data base. The interface, constructed by M. Read, recorded information input by our group in SQL format so they could be linked to the original data base entries for each galaxy. To this end, the interface showed scaled \$JHK\$ images from the 2MASS XSC (Jarrett et al. 2000) and $b_J r_F$ images from SuperCOSMOS (Hambly et al. 2001). These images were displayed alongside the redshifted labelled spectrum for the galaxy (example shown in Fig. 15).

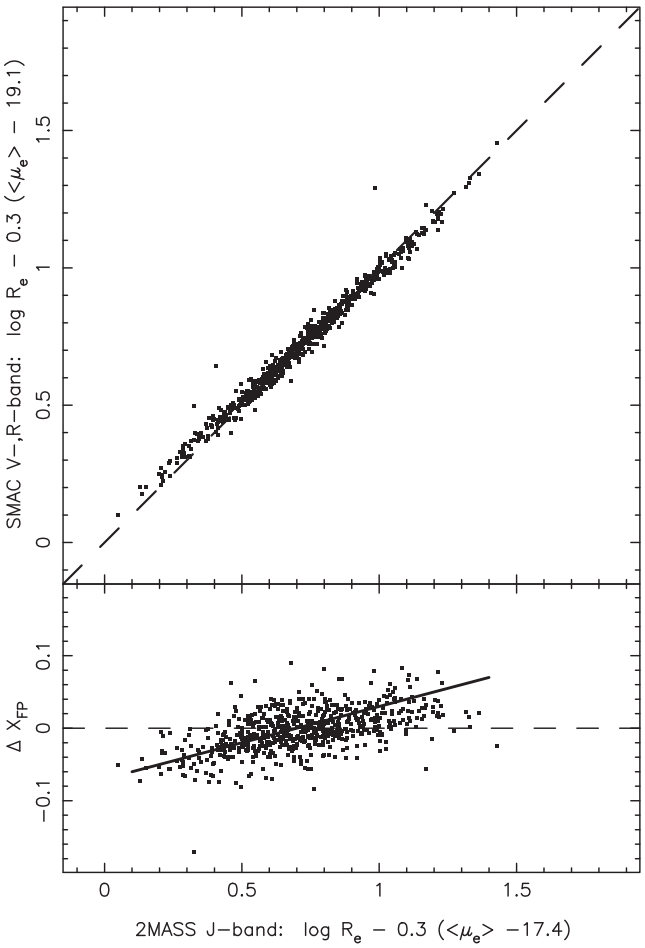

Figure 13. Comparison of the X_{FP} for the 2MASS *J*-band and SMAC *V*-, *R*-band measurements. To aid the comparison, the average effective surface brightness for the sample in each band has been subtracted from $\langle\mu_e\rangle$. For this comparison, we include corrections to the effective surface brightnesses for galactic extinction, the *k*-correction and cosmological surface brightness dimming. The rms scatter of the difference is 0.027 dex. The residual trend (lower panel) is a direct result of the colour–magnitude relation and is detected at high significance. The slope of the $J-(V,R)$ colour–magnitude for the SMAC sample is ∼0.1, and a line of slope 0.1 is shown in the lower panel, i.e. this is the expected systematic trend that would result from the observed colour–magnitude relation.

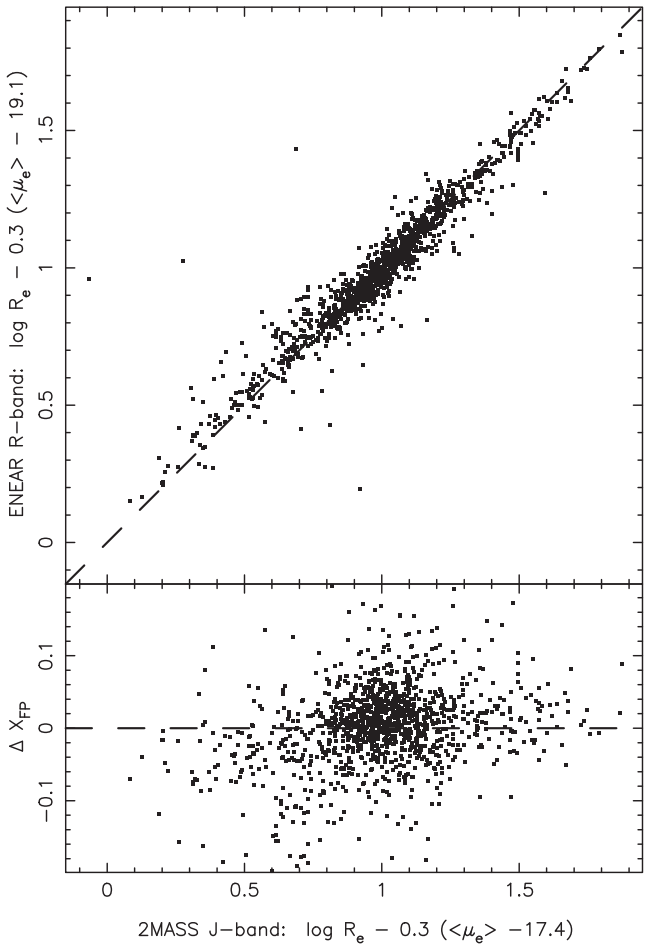

Figure 14. Comparison of the X_{FP} for the 2MASS *J*-band and ENEAR *R*-band measurements. To aid the comparison, the average effective surface brightness for the sample in each band has been subtracted from $\langle\mu_e\rangle$. For this comparison, we include corrections to the effective surface brightness for galactic extinction, the *k*-correction and cosmological surface brightness dimming. The rms scatter of the difference is 0.047 dex.

The classification work was undertaken by 10 members of the 6dFGS project team[1] and was organized to maximize the number of galaxies viewed and classified independently by at least two people. Fig. 16 shows the number of galaxies viewed a given number of times by independent classifiers. It shows that there were 9226 galaxies (83 per cent of the full sample) classified two or more times. Repeating the classifications using different people for most of the sample means that the dispersion in the type assignments can be used as a measure of self-consistency.

Our classification scheme was modelled on the one used by Dressler (1980), who targeted galaxies over comparable distances with similar resolution and sensitivity. Like all modern qualitative schemes, ours was based on the de Vaucouleurs (1959) revision of Hubble's original morphological sequence (Hubble 1926). Although we did not distinguish between barred and normal spirals, we did separate galaxies into the major categories of elliptical (E), lenticular (S0), spiral (Sp) and irregular (Irr) types, as well as intermediate cases (e.g. Sandage 1961; Jarrett 2000).

Table 5 lists the classification divisions used in our analysis. We assigned numerical values (called *m*-types) running from −4 to +6 on a scale of our own invention. Galaxy *m*-types (*m* for morphology) differ from other numerical classification schemes (notably *T*-types) in the way that galaxy orientation was encoded. The problem is not so much orientation per se, but the way in which the inclination affects different types disproportionally: disc galaxies are more likely to be misclassified at high inclination angles because of their flattened shape.

The established morphological *T*-type scale (de Vaucouleurs, de Vaucouleurs & Corwin 1976; Simien & de Vaucouleurs 1986) assigns values from −6 for ellipticals up to +7 for late-type spirals (Sc/Sd) and beyond (≥8) for irregular galaxies. Negative *T*-types refer exclusively to early types (ellipticals/lenticulars) while late types (spirals/irregulars) have positive values. Fukugita et al. (2007) used their own variation on *T*-types with a scale from 0 to 6 (with −1 reserved for unclassifiable objects).

[1] Beutler, Cluver, Colless, Jarrett, Jones, Lucey, Magoulas, Mould, Parker and Springob.

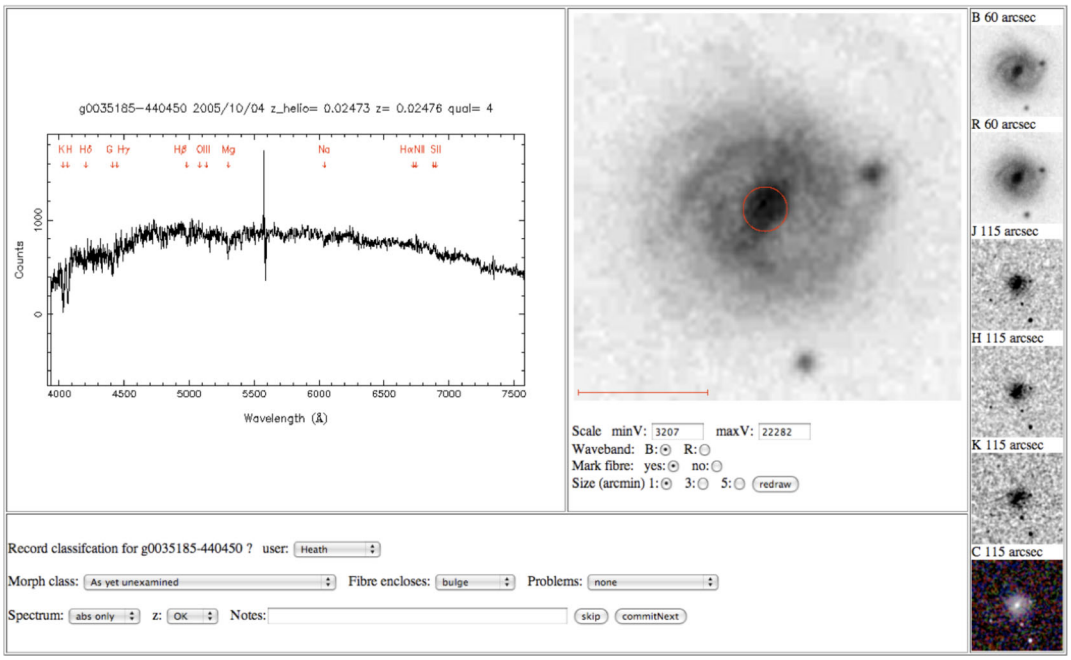

Figure 15. Purpose-built interface used to morphologically classify galaxies. The example shown is the nearby barred-spiral ESO 242−G 017 ($z = 0.024\,73$). This galaxy is an example of a late-type system with a bulge that fills the 6dF fibre aperture, giving an early-type spectrum with negligible line emission.

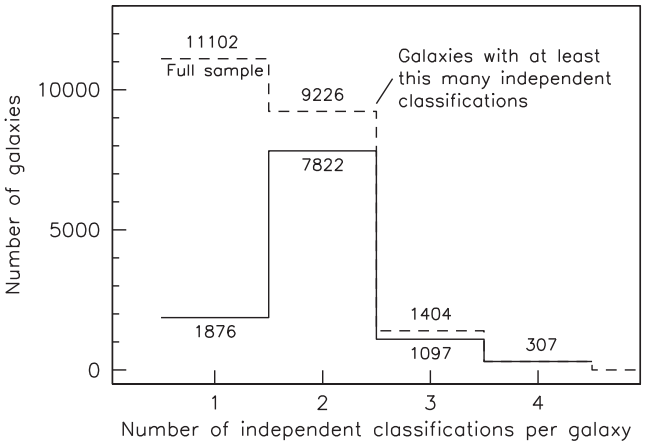

Figure 16. Differential (solid) and cumulative (dashed) distributions of the number of galaxies with a given number of morphological classifications. By *classifications*, we mean the number of times an individual galaxy was independently viewed and assessed by one of our group. The cumulate runs from right to left and represents the number of sample galaxies having at least that number of independent classifications.

Table 5. Morphological classification of the 6dFGSv.

Morphology	*m*-type
Edge-on disc galaxy with full-length dust lane	−4
Edge-on disc galaxy with partial or no dust lane	−2
Elliptical	0
Transition case: Elliptical – S0	+1
S0 (inclined/face-on)	+2
Transition case: S0 – Spiral	+3
Spiral (inclined/face-on)	+4
Transition case: Spiral – Amorphous	+5
Irregular or amorphous	+6
Unclassifiable	*999*

A galaxy in our scheme with $m = 0$ is an ordinary elliptical. Unambiguous, low-inclination-angle ($i \lesssim 60^\circ$) disc galaxies were assigned $m = +2$ in the case of lenticulars (S0s) and $m = +4$ for ordinary spirals. No attempt was made to subdivide spirals into early and late types. Irregular galaxies were allocated $m = +6$. Face-on and low-inclination S0s are distinguished from Es by the presence of a bulge. For the purpose of deriving a clean FP, our ability to distinguish spirals from S0s is paramount, much more so than separating S0s and ellipticals.

The intermediate odd-numbered values ($m = +1, +3, +5$) were used to denote the transition or intermediate cases between the key types. Transition galaxies are those that are ambiguous in appearance, regardless of whether this reflects their true nature. Because of this, our use of the word *transitional* is not meant to imply anything about how galaxies evolve.

Most importantly, negative *m*-types were reserved for edge-on cases (inclination angles $i \gtrsim 60^\circ$) where the galaxy has an obvious disc but its nature as an S0 or spiral is ambiguous. Galaxies with $m = -4$ were edge-on cases with an obvious dust lane, while $m = -2$ is given to those edge-on cases with no obvious dust lane. Although our use of optical $b_J r_F$ imaging facilitated these distinctions, edge-on dust lanes are not an unequivocal indicator of spiral structure. However, the *m*-type scheme incorporates this limitation by allowing edge-on cases to be flagged.

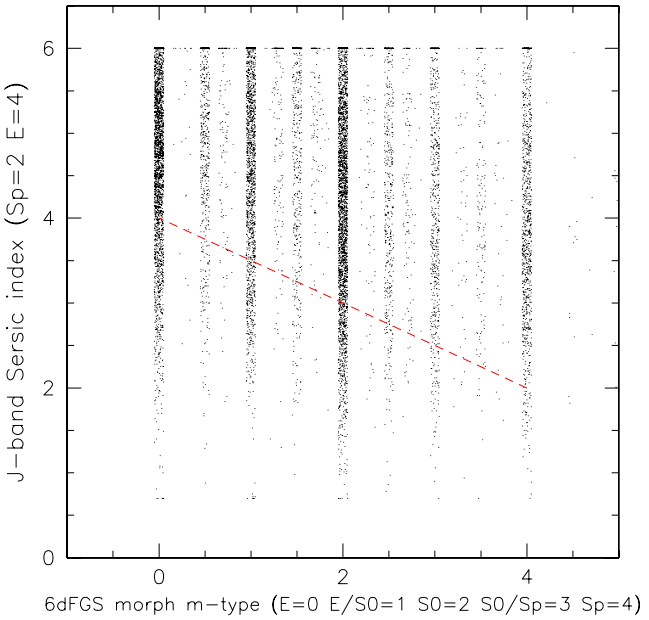

Figure 17. Comparison of visual morphological classification and *J*-band Sérsic. The trend of Sérsic index of 4 for ellipticals to 2 for spirals (bulges) is shown as the dashed line.

The utility of the *m*-type scheme is that it makes provision for inclination while simultaneously preserving classification information. By defining $|m|$-type as the absolute value of the *m*-type, edge-on disc galaxies (with $m = -2, -4$) are readily combined with all other disc galaxies in the sample (values $m = +2, +4$) if one so chooses. Alternatively, if we want to remove the edge-on cases entirely, we can do that by simply restricting the sample to $m \geq 0$.

The advantages of this approach were twofold. First, it acknowledges the unavoidable role played by inclination by incorporating it into the classification scheme. Secondly, it affords a simple way of differentiating between galaxies for which orientation has played a role from those of the same morphological type on a surer footing. In this way, we deferred any decision about whether a particular classification was incorporated into our final sample. This ensured that the decision-making process imposed on classifiers was kept as simple as possible, enabling a speedy and consistent classification of thousands of galaxies. Problem cases were also tagged, ensuring a clean final sample. There were 389 galaxies (3.5 per cent of the sample) for which two or more classifiers flagged a problem.

As an alternative indicator of morphological type, we considered using our GALFIT-derived *J*-band Sérsic indices (see Table 4). While there is a trend of decreasing Sérsic index as the morphological type changes from elliptical to spiral, the scatter is large (see Fig. 17). The low signal-to-noise of the 2MASS image data and the bulge-dominated nature of the NIR light make these 2MASS-based Sérsic indices a poor discriminator of morphological type and therefore the indices were not used for the selection of our FP sample.

All galaxies were also assessed according to three quality controls, and a code was assigned in each case (Table 6). The three aspects were as follows.

(i) *Fibre coverage of the galaxy:* whether the fibre aperture was dominated by light from the bulge alone, a disc (with little or no bulge), or a combination of the two. By *dominated* we mean that the estimated bulge contribution to the observed spectrum was >80 per cent. By *little or no* we mean that the bulge contribution was estimated at <20 per cent.
Fig. 15 shows an example of a nearby barred-spiral galaxy where the bulge fills the fibre aperture, giving an early-type spectrum for a late-type galaxy.

(ii) *Source confusion:* flagging cases of galaxy/galaxy or galaxy/star overlap (within or adjacent to the fibre aperture), or other special cases of note (e.g. Galactic sources, high-redshift QSOs).

(iii) *Spectral nature:* broadly characterizing whether the spectrum was dominated by absorption or emission-line features, or both. In addition, at this stage redshifts were checked for gross errors (none were found).

Table 6. 6dFGS quality control classification codes for (1) fibre coverage, (2) source confusion and (3) spectral features.

Fibre coverage	Code	Description
Bulge	1	Bulge is present (S0-Sp) and it fills the fibre aperture, or the galaxy has no disc (E)
Disc	2	Galaxy shows no bulge (Irr), or fibre misses bulge completely
Bulge+disc	3	Fibre captures light from both bulge and disc, or the galaxy is an edge-on disc
Source confusion	Code	Description
None	1	–
Galaxy+star	2	The light in the fibre has contributions from a nearby star
Galaxy+galaxy	3	The light in the fibre has contributions from two or more galaxies
Not a galaxy	4	The fibre light is dominated by a star/PN/H II region/QSO
Other	5	Any problem not fitting the above
Spectral features	Code	Description
Absorption only	1	Galaxy continuum with only clearly discernible absorption features
Absorption+emission	2	Both absorption and emission features clearly discernible above the noise
Emission only	3	Little or no detected continuum and no discernible absorption features, or absorption features of much lower prominence than emission lines

4.2 Results

Fig. 18 summarizes the results of our morphological classification for the full 6dFGSv sample. The final *m*-type for a given galaxy was the average of the individual values assigned by the classifiers for that galaxy. The number of galaxies for each type is shown, divided into bins of $|m|$-type, which has the aforementioned property of merging the edge-on cases with all other disc galaxies. There were 1712 galaxies (15 per cent of the sample) classified as edge-on by at least half of the people viewing each one.

The sample was dominated by elliptical and S0 types (9291 galaxies with $|m| < +3$, or 84 per cent of the full sample). This was not unexpected, since the input sample was selected by spectroscopic

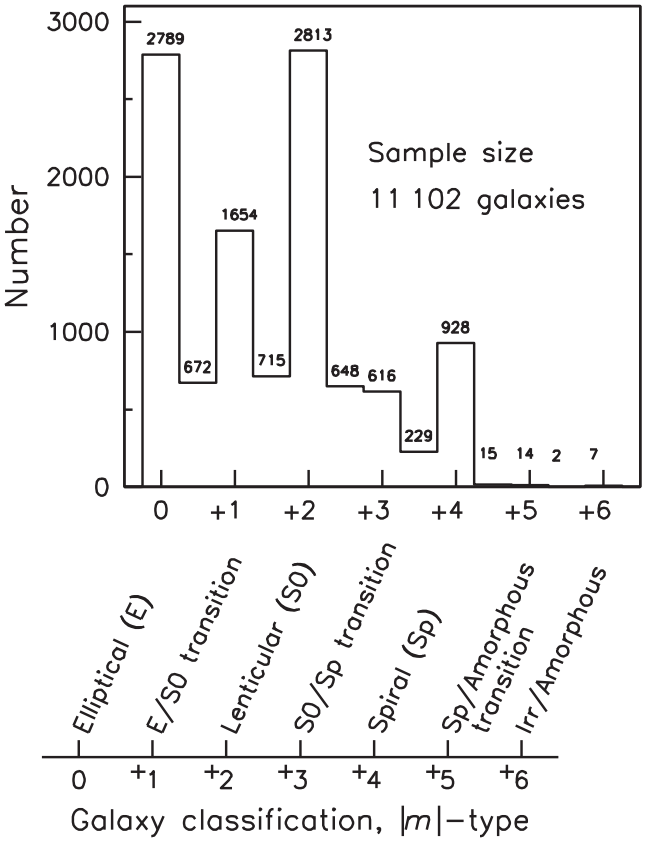

Figure 18. Distribution of galaxy types assigned to the 6dFGSv sample, binned by $|m|$-type (i.e. the absolute value of m-type). The lower axis gives the relationship between $|m|$-type and morphology. The counts at the half-classification step arise due to the effect of averaging integer classifications over multiple observations.

matching to early-type galaxy template spectra. Importantly, Fig. 18 also shows a small but non-negligible number of spirals (928 galaxies or 8 per cent). This was also not surprising, since these are cases where the bulge of the spiral fully fills the fibre aperture. As noted above, fibre coverage was one of the quality control parameters noted for each galaxy independently of morphology (Table 6). Fig. 18 also shows that transitional cases are relatively few. We do not believe that this reflects the true occurrence of these systems, as the effect of increased distance blurs the distinction between different galaxy types.

The simplest internal consistency check we used was to examine the dispersion, $\sigma(|m|)$, in $|m|$-types assigned by all classifiers for a given galaxy. Cases of full agreement between classifiers should result in zero dispersion. Fig. 19 shows the number of galaxies in bins of $\sigma(|m|)$, excluding the 1897 with only one classification. Over 93 per cent of the sample has a classification dispersion of less than a single class ($\sigma(|m|) \leq 1$), including 4629 galaxies with zero dispersion. A dispersion of less than two classes ($\sigma(|m|) \leq 2$) encompasses 99.8 per cent of the sample. Given that the major types (elliptical/S0/spiral) are all separated by $|m|$-type intervals of +2, Fig. 19 demonstrates our self-consistency in distinguishing the major types from one another for the vast majority of the 6dFGSv sample.

The effects of increasing distance complicated the task of galaxy classification in two ways. We divide these into imaging and spectroscopic classification biases.

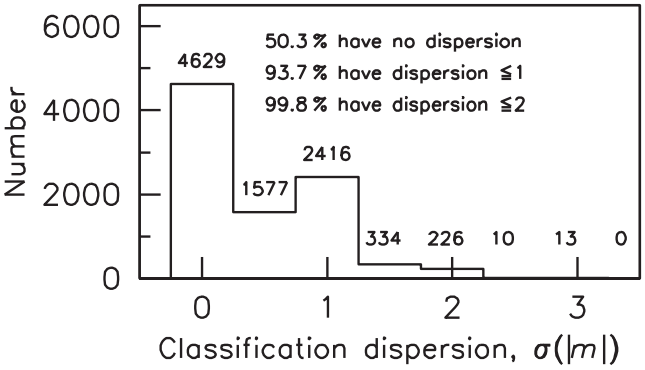

Figure 19. Distribution of the dispersion in the $|m|$-type values assigned independently. The subsample shown excludes the 1897 galaxies with only a single classification, which have $\sigma = 0$ by default.

Imaging classification bias relates to the increasing difficulty of recognizing a galaxy type at the sensitivity and spatial resolution limits of the system. Faint and detailed structures such as spiral arms and dust lanes demand the most stringent imaging requirements. As a consequence, galaxy classification schemes based purely on imaging tend to increasingly misclassify late-type galaxies as early types at higher redshifts. This effect is evident in large catalogues such as Galaxy Zoo (e.g. Bamford et al. 2009), where the number of unequivocal spirals (in the sense that more than 80 per cent of the classifiers agreed) seen at redshift $z \sim 0.08$ was half the number seen at $z \sim 0.01$, while over the same interval the number of ellipticals doubles. Obviously, this is a major concern for surveys considering morphology in the absence of other (e.g. spectral) information; fortunately, this was not the case for 6dFGSv.

Spectroscopic classification bias arises when galaxy types are assigned on the basis of their spectra through a fixed aperture. Such apertures are almost always circular and positioned over the galaxy centre, meaning that light from the outer regions is only sampled in the cases where the galaxy is sufficiently small and/or distant. This means that a sample ostensibly of early types can in fact contain late-type galaxies whose proximity ensures that the bulge fills the fibre aperture, producing an early-type spectrum. Clearly, this effect is distance dependent.

Both forms of bias act to underestimate the numbers of spirals in different redshift regimes. Spectroscopic classification bias operates at lower redshifts while imaging classification bias tends to be an issue at higher redshifts. However, since we were concerned with constructing an FP sample of early types, biases that act to miss late types were not important. The only effect we concerned ourselves with was late types being mistaken for early types as a consequence of spectroscopic classification bias. This bias was present in 6dFGSv but was also readily identifiable: our visual screening of the galaxy images ensured that spiral bulges were identified correctly. As the 6dFGSv sample was limited to redshifts $z < 0.055$, image classification bias was limited, as experience showed that reliable classification is possible to an apparent magnitude limit of $K \sim 13$ (or equivalently, $b_J \sim 17$). A more stringent test was to examine the composition of our sample with increasing distance.

These effects were explored by measuring the distribution of types in terms of surface brightness and redshift. The surface brightness distributions in Fig. 20 tended towards fainter values for spirals and spiral transition cases. This was not unexpected given the initial preselection of our sample based on bulge spectral properties. At a fixed luminosity, a spiral galaxy will, due to its disc, have a

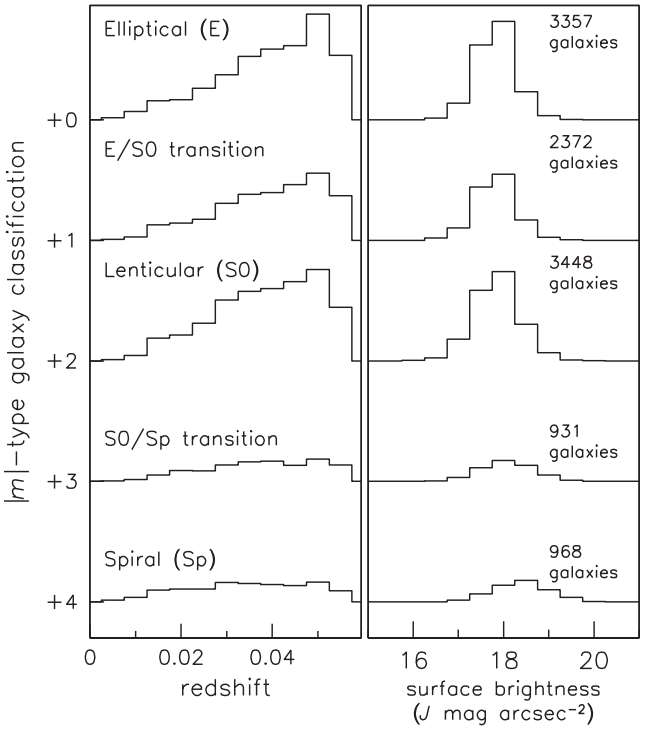

Figure 20. Galaxy distribution in each $|m|$-type classification bin as a function of redshift (left) and surface brightness (right).

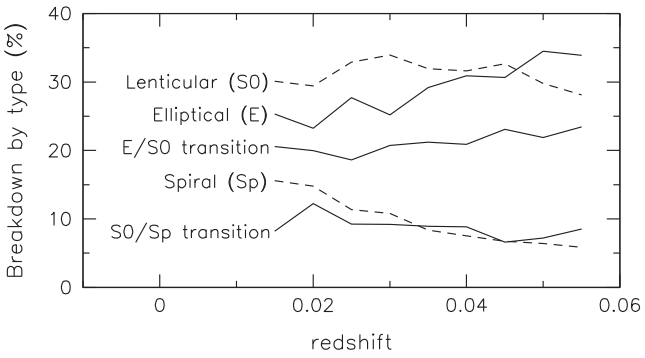

Figure 21. Relative galaxy number as a function of redshift.

lower overall surface brightness than an elliptical. The fact that the range of surface brightness seen in Fig. 20 does not change more was likely due to our preference for early types where total galaxy luminosity was dominated by the contribution from the bulge over the light from any disc.

Fig. 21 shows that the mix of types found by our classification scheme did not change appreciably over the redshift range considered. We recorded a small rise in the fraction of ellipticals (from 25 to 35 per cent) while the numbers of S0s and transition cases remained constant. We attribute the corresponding decline in the number of spirals (from 15 to 6 per cent) to two effects. First, the fact that the fraction of early types increases with luminosity means that they will also increase with redshift in a magnitude-limited sample. Secondly, the spectroscopic preselection (and the fixed fibre aperture employed) will include the very lowest redshift spirals because of the early-type appearance of their bulge-dominated spectra. At higher redshifts, the spirals are spectroscopically rejected as more of the fibre aperture flux is due to the light of the star-forming discs, including emission lines from the H II regions. This emphasizes the

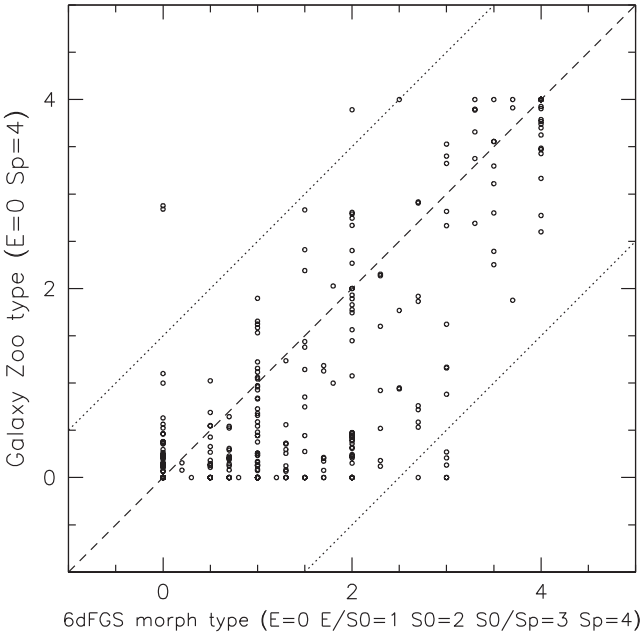

Figure 22. Comparison of Galaxy Zoo (Lintott et al. 2008) and 6dFGS morphological types for a sample of 281 galaxies in common. The Galaxy Zoo classification has been transformed to the 6dFGS scheme indicated on the horizontal axis. The dashed line shows the 1:1 relation and the dotted lines show the (+1.5, −2.5) boundaries that encompass most of the scatter. Galaxy Zoo classifications have a tendency towards earlier types.

importance of our visual screening to counter the spectroscopic classification bias inherent in the input sample.

The other check we used was to benchmark our classifications against those of another group. We made a comparison between Galaxy Zoo morphological types and our assignments for the sample of 281 galaxies common to both. Galaxy Zoo (Lintott et al. 2008) is the compilation of basic morphological typing obtained by crowd-sourcing the visual classification of 893 212 galaxies from the Sixth Data Release of the Sloan Digital Sky Survey (Adelman-McCarthy et al. 2008). For the Galaxy Zoo sample, there was a median of 34 independent views per galaxy using elliptical and spiral as the two main classification divisions.

Fig. 22 shows the comparison between the 6dFGSv and Galaxy Zoo. To facilitate comparison, we rescaled the combined Galaxy Zoo type on an equivalent scale of 0 to 4 (elliptical to spiral). Edge-on and problem cases have been excluded from the sample, as have galaxies with only one independent classification. The agreement between 6dFGSv and Galaxy Zoo is good with minimal scatter ($\sigma(|m|) \sim 1$). The amount of scatter about the 1:1 relation is less than the size of the step ($\Delta|m| = 2$) separating the major galaxy classes (E:S0:Sp).

However, Fig. 22 also shows a tendency towards early typing by Galaxy Zoo relative to the 6dFGSv classes, in that a greater number of galaxies lie below the 1:1 line. We contend that this was due to the redder optical passbands used by Galaxy Zoo, and their reliance on composite images rather than examination of separate images in each passband. Morphological typing of 6dFGSv galaxies was done using multiple independent optical images ($b_J r_F$), with supporting NIR *JHK* frames and a colour NIR composite. In contrast, Galaxy Zoo classifications used only a single-colour composite image made from optical *gri* passbands. Since none of these sample the galaxy light shortwards of $\lambda \lesssim 4000$ Å, the blue light of the OB stars that dominate the arms of spiral galaxies is under-represented in the

composite frames. Therefore, galaxies with fainter spiral features tend to be classified as S0s (predominantly on the basis of their bulge).

The morphological classifications of 6dFGSv were used for both trimming problem galaxies and examining FP trends with morphology (Magoulas et al. 2012). The characteristics of this morphologically clean sample are discussed below.

5 6DFGSV FP SAMPLE

In this section, we describe how the 6dFGSv FP sample and catalogue are constructed from the measurements described in previous sections.

5.1 Velocity dispersion aperture correction

Our measured velocity dispersions (σ) are corrected to a standard physical aperture size of $R_e/8$, using the empirically derived formula given by Jorgensen et al. (1995b):

$$\frac{\sigma_0}{\sigma} = \left(\frac{R_e/8}{R_{ap}}\right)^{-0.04}, \quad (7)$$

where σ_0 is the 'central' velocity dispersion within a circular aperture of radius $R_e/8$. The 6dF fibre diameter is 6.7 arcsec and so $R_{ap} = 3.35$ arcsec. Rather than using the above equation directly with our NIR-based R_e measurements, we first use an empirical relation that maps R_e(NIR) to R_e(optical) in order to provide a closer match to previous optical-based studies.

Using a sample of galaxies in common with the ENEAR survey (Alonso et al. 2003), we derived the following relation between the *R*- and *J*-band effective radii

$$\log R_e^R = 1.029 \log R_e^J + 0.140. \quad (8)$$

The range of R_e^J for our sample is 1.6–16 arcsec, corresponding to an R_e^R range of 2.2–24 arcsec. The correction factor to the measured velocity dispersion ranges from 1.107 to 1.010.

5.2 R_e and $\langle I_e \rangle$

We convert the effective radii R_e in arcseconds, as given in Table 4, to effective radii R_e^{kpc} in physical units of h^{-1} kpc using

$$\log R_e^{kpc} = \log R_e + \log D_A + \log(1000/206\,265), \quad (9)$$

where D_A is the galaxy's angular diameter distance in units of h^{-1} Mpc derived from the measured galaxy redshift [in the local cosmic microwave background (CMB) rest frame] using a flat cosmology with $\Omega_m = 0.3$, $\Omega_\Lambda = 0.7$ and $H_0 = 100\,h\,\mathrm{km\,s^{-1}\,Mpc^{-1}}$.

We find that 3186 of the galaxies in the sample are members of groups, as identified by the friends-of-friends grouping algorithm outlined by Magoulas et al. (2012). For these galaxies, we use the redshift of the group, rather than the individual galaxy redshift, to compute the redshift distance and the corresponding physical radius. The group redshift is defined as the median redshift of all galaxies in the group.

Corrections were made to the values of $\langle \mu_e \rangle'$ for (i) the cosmological surface brightness dimming, (ii) the *k*-correction, using the approximations of $+0.7z$, $+0.2z$ and $-3.3z$ mag for the *J*, *H* and *K* bands, respectively (Persson, Frogel & Aaronson 1979), and (iii) galactic extinction using the values given by Schlafly & Finkbeiner (2011) as reported by NASA/IPAC Extragalactic Database. The fully corrected effective surface brightness is calculated as

$$\langle \mu_e \rangle = \langle \mu_e \rangle' - 2.5 \log(1+z)^4 - k_\lambda - A_\lambda, \quad (10)$$

where we use the redshift in the local CMB rest frame.

It is most natural to have all FP parameters in logarithmic units, so surface brightness values were converted from magnitude units (i.e. $\langle \mu_e \rangle$ in mag arcsec^{-2}) to log-luminosity units (i.e. $\log \langle I_e \rangle$ in $L_\odot$ pc^{-2}) using

$$\log\langle I_e \rangle = 0.4\,M_\odot^\lambda - 0.4\langle \mu_e \rangle + 2\log(206\,265/10), \quad (11)$$

where the absolute magnitude of the Sun, $M_\odot^\lambda$, depends on the passband. For the *J* band, $M_\odot^J = 3.67$, for the *H* band, $M_\odot^H = 3.33$ and for the *K* band, $M_\odot^K = 3.29$; these values for the absolute magnitude of the Sun are taken from http://mips.as.arizona.edu/~cnaw/sun.html.

5.3 Construction of the 6dF FP sample

By combining both the velocity dispersion measurements from Table 2 (with the above aperture correction) and 2MASS photometric measurements from Table 4 (with the corrections and conversion given above), we construct the 6dF FP sample.

It is important to distinguish between four overlapping samples used in our analysis. There are the three samples used to fit the FP, i.e. the *J*-, *H*- and *K*-band FP samples, while the fourth is the *J*-band sample used for the peculiar velocity analysis. Details of the galaxy selection for the latter are described in detail in Magoulas et al. (2012), and only a brief summary is given here.

In Section 2.4, we described an initial set of selection criteria on the velocity dispersion sample ($S/N > 5$, $R > 8$, $\sigma > 100\,\mathrm{km\,s^{-1}}$) that resulted in a sample of 11 315 galaxies. In Section 3, we reported photometric parameters for 11 102 of these galaxies. This is the parent sample from which additional selection cuts were made to produce a sample suitable for the FP analysis. These additional cuts are listed in Magoulas et al. (2012, table 1). We first limited the sample to galaxies with $3000 \leq cz_{CMB} \leq 16\,120\,\mathrm{km\,s^{-1}}$ and $\log\sigma_0 \geq 2.05$ (the latter cut is imposed rather than the original $\log\sigma_0 = 2.00$ to ensure a uniform limit after the aperture correction was applied). We also eliminated galaxies on the basis of the visual classification of the morphology described in Section 4; galaxies were excluded if at least one of four conditions was met: (i) galaxy morphology classified as irregular or amorphous; (ii) galaxy identified as edge-on with a full dust lane; (iii) significant fraction (>80 per cent) of the light in fibre is from the disc; or (iv) light in fibre is contaminated by nearby star, galaxy or defect.

These selection cuts resulted in a sample of 9656 galaxies. From that sample, we constructed individual *J*-, *H*- and *K*-band samples by imposing additional apparent magnitude cuts in each of the three bands. Our sample had slightly brighter flux limits than the original 6dFGS magnitude limits (Jones et al. 2009), reflecting the changes in the 2MASS (and, consequently, 6dFGS) magnitude limits that occurred after the 6dFGS sample was selected. To maintain high completeness in each passband over the whole sample area, we imposed magnitude limits of $J \leq 13.65$, $H \leq 12.85$ and $K \leq 12.55$.

In our FP fitting procedure, each galaxy was weighted by the inverse of its selection probability. This means galaxies are weighted by $1/S$, where S is the fraction of the survey volume in which a galaxy of that absolute magnitude could have been included in the sample. For each of the three photometric bands, we excluded galaxies for which $S < 0.05$ in order to prevent a small number of heavily weighted galaxies from strongly biasing the FP fit. Magoulas et al. (2012) also defined a χ^2 statistic, computed for each galaxy, which measured the galaxy's deviation from the model FP relation. Galaxies with χ^2 values greater than 12, representing a deviation from

Table 7. Summary of 6dFGS FP sample parameters. For each parameter, the table below lists its name, units and a short description. Units enclosed by brackets are logarithmic quantities.

Table column	Parameter	Unit	Description
(1)	6dFGSid	–	Source name in the 6dFGS catalogue
(2)	2MASSid	–	Source name in the 2MASS XSC catalogue
(3)	RA	degree	Right ascension (J2000)
(4)	Dec.	degree	Declination (J2000)
(5)	$cz_{\rm CMB}$	$\rm km\,s^{-1}$	CMB frame galaxy redshift
(6)	$\log R_{\rm e}^{\rm kpc}(J)$	[kpc h^{-1}]	Logarithm of effective radius in the J band
(7)	$\epsilon_{\log R_{\rm e}^{\rm kpc}(J)}$	[kpc h^{-1}]	Error in $\log R_{\rm e}^{\rm kpc}(J)$
(8)	$\log R_{\rm e}^{\rm kpc}(H)$	[kpc h^{-1}]	Logarithm of effective radius in the H band
(9)	$\epsilon_{\log R_{\rm e}^{\rm kpc}(H)}$	[kpc h^{-1}]	Error in $\log R_{\rm e}^{\rm kpc}(H)$
(10)	$\log R_{\rm e}^{\rm kpc}(K)$	[kpc h^{-1}]	Logarithm of effective radius in the K band
(11)	$\epsilon_{\log R_{\rm e}^{\rm kpc}(K)}$	[kpc h^{-1}]	Error in $\log R_{\rm e}^{\rm kpc}(K)$
(12)	$\log \langle I_{\rm e}\rangle\,(J)$	[$\rm L_\odot\,pc^{-2}$]	Logarithm of mean J-band surface brightness within $R_{\rm e}(J)$
(13)	$\epsilon_{\log\langle I_{\rm e}\rangle(J)}$	[$\rm L_\odot\,pc^{-2}$]	Error in $\log \langle I_{\rm e}\rangle\,(J)$
(14)	$\log \langle I_{\rm e}\rangle\,(H)$	[$\rm L_\odot\,pc^{-2}$]	Logarithm of mean H-band surface brightness within $R_{\rm e}(H)$
(15)	$\epsilon_{\log\langle I_{\rm e}\rangle(H)}$	[$\rm L_\odot\,pc^{-2}$]	Error in $\log \langle I_{\rm e}\rangle\,(H)$
(16)	$\log \langle I_{\rm e}\rangle\,(K)$	[$\rm L_\odot\,pc^{-2}$]	Logarithm of mean K-band surface brightness within $R_{\rm e}(K)$
(17)	$\epsilon_{\log\langle I_{\rm e}\rangle(K)}$	[$\rm L_\odot\,pc^{-2}$]	Error in $\log \langle I_{\rm e}\rangle\,(K)$
(18)	$\log \sigma_0$	[$\rm km\,s^{-1}$]	Logarithm of aperture-corrected central velocity dispersion
(19)	$\epsilon_{\log\sigma_0}$	[$\rm km\,s^{-1}$]	Error in $\log \sigma_0$
(20)	m-type	–	Average morphological type classification, see Table 5
(21)	GroupID	–	Group or cluster identification number
(22)	N_r	–	Richness of galaxy group or cluster
(23)	$cz_{\rm group}$	$\rm km\,s^{-1}$	Group or cluster median CMB redshift
(24)	d_5	Mpc h^{-1}	Projected comoving distance to the fifth nearest neighbour (not available for 1165 galaxies)
(25)	Σ_5	gals $\rm Mpc^{-2}\,h^2$	Surface density measured to the fifth nearest neighbour (not available for 1165 galaxies)
(26), (28), (30)	Sample code	–	The selection criteria that a galaxy satisfies are encoded in this sample code (*JHK*). These codes are six-digit binary strings, where digit = 0 or 1 indicates that the galaxy fails or satisfies the selection criterion. The six selection criteria (in left to right string order) are (1) $\log\sigma_0 > 2.05$; (2) $cz > 3000$ and $cz < 16\,120\,\rm km\,s^{-1}$; (3) morphological classification acceptable; (4) apparent magnitude <13.65 (J), 12.85 (H) or 12.55 (K); (5) selection probability >0.05 (*JHK*); (6) $\chi^2 < 12$ (*JHK*)
(27), (29), (31)	PV code	–	Code to indicate whether galaxy excluded from (0) or included in (1) the *JHK* 6dFGSv sample

the model of more than about 3.5σ, were also eliminated from the sample.

After applying these selection criteria, we obtained J-, H- and K-band samples of 8803, 8472 and 8461 galaxies, respectively. However, once the FP has been fitted, there are various FP applications for which it is appropriate to include some of the discarded galaxies, e.g. galaxies excluded by the lower redshift limit of $cz_{\rm CMB} = 3000\,\rm km\,s^{-1}$ and the selection probability limit of $S = 0.05$. In Springob et al. (2014), for example, we present the derivation of galaxy distances and peculiar velocities for the 6dFGSv sample. This is the sample of galaxies for which we have derived distances and peculiar velocities from the J-band data, and it includes these low-redshift and low-selection-probability galaxies, resulting in a total of 8885 objects in the peculiar velocity sample. The parameters derived for each galaxy in these overlapping samples are summarized in Table 7; the data table is given as Table 8.

Most of the parameters in this table have already been defined in this paper; however, we elaborate here on columns (21)–(31). As explained in Section 5.2, we make use of a group catalogue explained in Magoulas et al. (2012), which is drawn from the much larger set of all galaxies with redshifts in 6dFGS, not just those in the FP sample. Column (21) is the group ID number for the galaxy in question, in those cases for which the galaxy is in a group. We also define N_r in column (22) as the group richness. Because the faintest members of a group might not have been observed, the richness of a group is defined as the number of observed galaxies in the group brighter than a specified absolute magnitude, chosen so that galaxies brighter than this would be visible throughout the sample volume. Column (23) is the redshift of the group, taken as the median redshift of all galaxies in the group (including those within the 6dFGS redshift sample that are not in the FP subsample).

We also include two additional measures of local environment. Column (24) is the projected comoving distance to the fifth nearest neighbour (d_5) in h^{-1} Mpc. Column (25), the surface density (Σ_5), is defined using the projected comoving distance to the fifth nearest neighbour within $\pm 1000\,\rm km\,s^{-1}$ within a volume limited density-defining population with $M_K < -22$ mag. Further details of Σ_5 can be found in Brough et al. (2013).

Columns (26)–(31) are binary codes to denote whether or not a galaxy is included in the various subsamples previously described. For inclusion in a sample, six selection criteria are assessed. These are described in Table 7. Values in column (26) refer to the J-band data and are a six-character sequence which indicates which of the six selection criteria are met; 1 denotes inclusion and 0 denotes exclusion. Only galaxies with a value of 111111 in column (26) are included in the final J-band sample. Similarly, columns (28) and (30) give the six-character codes for the H-band and K-band data, respectively. Columns (27), (29) and (31) denote whether or not a galaxy is included in the J-, H- and K-band 6dFGSv peculiar velocity samples, respectively. As previously noted, we primarily used the J-band 6dFGSv sample for our peculiar velocity studies.

Table 8. The 6dFGS FP catalogue. Table 7 provides a description of each column. For ease of presentation here, the columns here are wrapped over three lines. Missing or not applicable values are set to −1, e.g. in column (21) for galaxies not assigned to a group. The full version of this table, with one galaxy per row, is provided in the online Supporting Information.

(1)	(3)	(4)	(5)	(6)	(7)	(8)	(9)	(10)	(11)		
(2)	(12)	(13)	(14)	(15)	(16)	(17)	(18)	(19)	(20)		
	(21)	(22)	(23)	(24)	(25)	(26)	(27)	(28)	(29)	(30)	(31)
g0000144-765225	0.059 85	−76.873 64	15941	0.465	0.057	0.363	0.069	0.261	0.092		
2MASXJ00001440−7652248	2.940	0.084	3.266	0.102	3.489	0.136	2.137	0.073	2.2		
	−1	−1	−1	4.2758	0.1176	111111	1	111111	1	111111	1
g0000222-013746	0.092 25	−1.629 47	11123	0.024	0.048	−0.010	0.057	−0.087	0.079		
2MASXJ00002213−0137463	3.708	0.071	3.921	0.085	4.067	0.118	2.338	0.023	2.5		
	−1	−1	−1	6.4318	0.0385	111111	1	111111	1	111111	1
g0000235-065610	0.097 80	−6.936 19	10920	0.343	0.047	0.370	0.057	0.133	0.083		
2MASXJ00002348−0656103	3.067	0.070	3.161	0.084	3.562	0.123	2.219	0.045	3.7		
	−1	−1	−1	6.2142	0.0448	111111	1	111111	1	111111	1
g0000251-260240	0.104 55	−26.044 50	14926	0.371	0.046	0.338	0.055	0.310	0.074		
2MASXJ00002509−2602401	3.328	0.068	3.531	0.082	3.592	0.110	2.369	0.040	2.3		
	−1	−1	−1	3.2827	0.1434	111111	1	111111	1	111111	1
g0000356-014547	0.148 50	−1.763 17	6956	0.316	0.042	0.286	0.052	0.320	0.067		
2MASXJ00003564−0145472	2.859	0.062	3.029	0.077	3.040	0.099	2.144	0.066	3.0		
	−1	−1	−1	3.8994	0.1036	111111	1	111111	1	111111	1

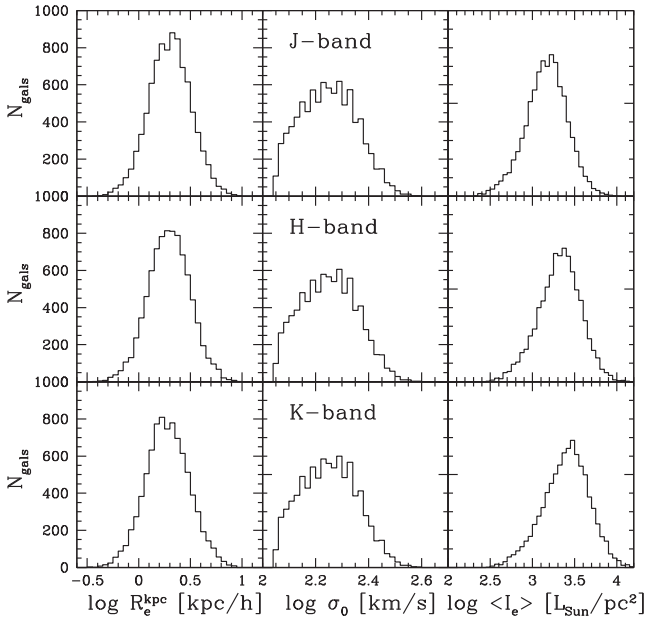

Figure 23. The distribution of the observed FP parameters, $\log R_e^{kpc}$, $\log \sigma_0$ and $\log \langle I_e \rangle$ for the *J*-, *H*- and *K*-band samples. The top row shows the histograms of the three parameters in the *J* band, the middle row those in the *H* band and the bottom row those in the *K* band. The $\log R_e^{kpc}$ and $\log \langle I_e \rangle$ values vary with passband for every galaxy, while the $\log \sigma_0$ value for each galaxy remains unchanged. However, the $\log \sigma_0$ histograms do vary slightly with passband, since the *J*-, *H*- and *K*-band samples include a slightly different mix of galaxies. Bin widths on $\log R_e^{kpc}$, $\log \sigma_0$ and $\log \langle I_e \rangle$ are 0.05, 0.02 and 0.05 dex, respectively.

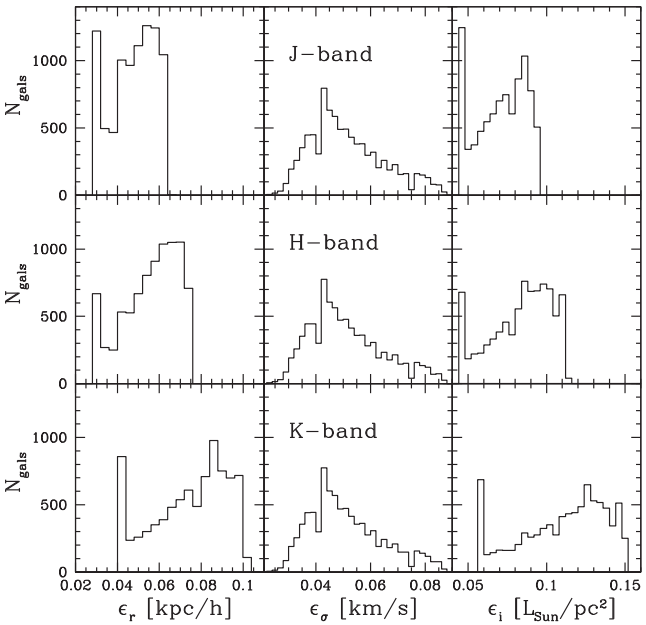

Figure 24. The distribution of the errors on the observed FP parameters $\log R_e^{kpc}$, $\log \sigma_0$ and $\log \langle I_e \rangle$ for the *J*-, *H*- and *K*-band samples (top to bottom). Bin widths on $\epsilon_{\log r}$, $\epsilon_{\log \sigma}$ and $\epsilon_{\log i}$ are 0.004, 0.002 and 0.004 dex, respectively.

In Fig. 23, we show histograms of $\log R_e^{kpc}$ and $\log \langle I_e \rangle$ for all three bands, as well as the histogram of $\log \sigma_0$. In Fig. 24, we show histograms of the errors on each of these quantities, while in Fig. 25 we show the histograms of redshifts for the *J*-, *H*- and *K*-band samples, as well as the peculiar velocity sample 6dFGSv (in the *J* band).

This is the first public release of the 6dFGS Fundamental Plane peculiar velocity catalogue (6dFGSv). In previous work (Magoulas et al. 2012; Springob et al. 2012), we used a preliminary version of this catalogue. Table 8 is an updated version of our original catalogue.

The main changes are (i) the inclusion of improved velocity dispersion errors, calculated via a bootstrap technique as described in Section 2.3 (previously these were derived using the TD79 error formula); (ii) after visually inspecting the 2MASS postage stamp images and the GALFIT residual images for all objects, exclusion of 129 galaxies where either the 2MASS processing removed a substantial part of the target galaxy (e.g. 2MASXJ08532460−0919124) or the presence of a strong core asymmetry indicated multiple structures (e.g. 2MASXJ13525793−4751401); (iii) improved masking

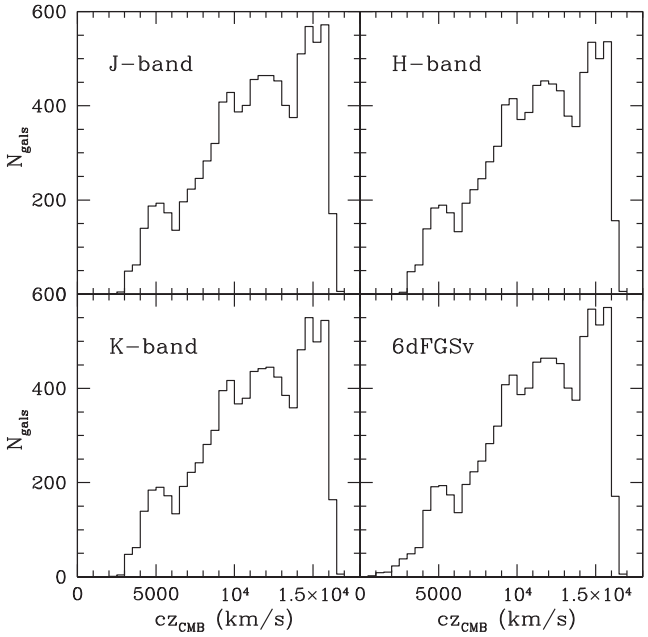

Figure 25. The redshift distributions for the *J* band (upper left), *H* band (upper right), *K* band (lower left) and the 6dFGSv peculiar velocity (lower right) samples. The bins have width 500 km s^{-1}.

of contaminating stars in the GALFIT analysis for ∼100 galaxies; (iv) the use of updated Galactic extinction values from Schlafly & Finkbeiner (2011) rather than from Schlegel, Finkbeiner & Davis (1998); and (v) recalculation of the individual galaxy sample codes as a result of the above changes to the input data set.

There are no substantive changes to the conclusions reached in our previous work when this updated 6dFGSv catalogue is used, as (apart from the new velocity dispersion errors) the changes to the data set are very small. In addition, our FP analysis procedure (see Magoulas et al. 2012) was robust, as outliers were iteratively culled. Further details are reported in Magoulas et al. (in preparation).

5.4 6dFGS stellar population parameters

For completeness we also present here, in Table 9, the stellar population parameters for the 6dFGSv sample that were derived in Proctor et al. (2008).

These stellar population parameters, which apply to the 6.7 arcsec diameter central region of each galaxy covered by a 6dF fibre, are based on Lick index measurements and the χ^2-fitting procedure of Proctor & Sansom (2002), which uses all available indices to obtain simultaneous estimates for log(age), [Fe/H], [*Z*/H] and [α/Fe]. This method is relatively robust against the problems that can afflict spectral index measurements, particularly when (as for 6dFGS) the spectra cannot be flux-calibrated, and also, to a certain extent, against uncertainties in the stellar population models. Here the models of Korn, Maraston & Thomas (2005) were used, as they provide the required range in both age and metallicity and include the effects of varying α-element abundances. For the passive galaxies in the FP sample, between 10 and 15 Lick indices ranging from Hδ to Fe5406 were included in the fits. Some indices in this wavelength range were excluded, however, because they were poorly fitted by the models: the Ca4455, Mg1 and Mg2 indices (which are sensitive to flux calibration), and the Hβ and Fe5015 indices (which suffer from low-level emission-line contamination).

For the passive galaxies in the FP sample, the mean reduced χ^2 was 1.08, indicating satisfactory fits given the measured errors in the Lick indices. For each galaxy, the errors in the stellar population parameters were estimated as the rms scatter in the values obtained from 50 Monte Carlo simulations of the fitting procedure using the observational errors in the Lick indices for that galaxy. Excluding low-S/N galaxies with errors in log(age) greater than 0.3 dex, for which the stellar population parameters are deemed unreliable, the mean errors in both log(age) and [*Z*/H] are approximately 0.15 dex. These errors depend on spectral S/N: for galaxies with S/N > 16 the mean errors in both quantities are ∼0.1 dex, while for S/N < 16 they are ∼0.2 dex. The errors in age and metallicity are, as usual, somewhat correlated. A quality parameter, $Q_{\rm SP}$, was also defined as the sum of the integerized reduced χ^2 and the number of clipped indices; galaxy spectra with a $Q_{\rm SP}$ value of 1 have the best quality fits. Only data from galaxies with S/N per angstrom greater than 9 and quality parameter of 10 or lower are used in our analysis, and included in Table 9. Proctor et al. (2008) consider all these issues in detail, and further discussion of the stellar population parameters and their effect on the FP is provided by Springob et al. (2012).

6 CONCLUSIONS

This paper reports the measurements of FP parameters for nearly 9000 galaxies in the 6dFGS peculiar velocity survey (6dFGSv) and

Table 9. 6dFGS stellar population catalogue. Only galaxies that meet the criteria S/N ≥ 9 Å^{-1} and $Q_{\rm SP}$ ≤ 10 are listed here (see Proctor et al. 2008). The columns are (1) source name in 6dFGS catalogue; (2) logarithm of the galaxy age in Gyr; (3) error in log age, $\epsilon_{\rm age}$; (4) Fe abundance, [Fe/H]; (5) error in [Fe/H], $\epsilon_{\rm Fe/H}$; (6) α-element overabundance ratio, [α/Fe]; (7) error in [α/Fe], $\epsilon_{\alpha/\rm Fe}$; (8) overall metallicity, [*Z*/H]; (9) error in [*Z*/H], $\epsilon_{Z/\rm H}$; (10) quality of the stellar population parameter fits, $Q_{\rm SP}$. The full version of this table is provided in the online Supporting Information.

6dFGS ID (1)	log age (2)	$\epsilon_{\rm age}$ (3)	[Fe/H] (4)	$\epsilon_{\rm Fe/H}$ (5)	[α/Fe] (6)	$\epsilon_{\alpha/\rm Fe}$ (7)	[*Z*/H] (8)	$\epsilon_{Z/\rm H}$ (9)	$Q_{\rm SP}$ (10)
g0000144-765225	0.650	0.088	−0.646	0.158	0.500	0.111	−0.175	0.063	5
g0000222-013746	0.500	0.058	0.435	0.066	−0.090	0.040	0.350	0.047	7
g0000235-065610	0.475	0.075	0.237	0.088	0.120	0.038	0.350	0.067	5
g0000251-260240	0.775	0.108	0.027	0.125	0.210	0.064	0.225	0.072	6
g0000356-014547	0.375	0.046	−0.070	0.073	0.180	0.046	0.100	0.045	5
g0000358-403432	0.500	0.107	0.005	0.151	0.180	0.070	0.175	0.099	8
g0000428-721715	1.175	0.021	−0.185	0.057	0.090	0.048	−0.100	0.030	4
g0000459-815803	0.250	0.042	−0.170	0.131	0.180	0.082	0.000	0.067	6
g0000523-355037	0.700	0.083	−0.471	0.113	0.500	0.073	0.000	0.054	8

describes how the FP catalogue was constructed. This is the largest and most homogeneous set of FP measurements for galaxies in the nearby universe obtained to date.

These data have previously been used to study the effects of stellar population differences on galaxy scaling relations (Proctor et al. 2008), to characterize the NIR FP and investigate trends in the FP with environment and galaxy morphology (Magoulas et al. 2012), and to map the changing stellar populations of galaxies as a function of their location within the FP (Springob et al. 2012).

In papers now in preparation, this catalogue will be exploited to derive FP distance estimates for these galaxies, and so determine the peculiar velocity field throughout the Southern hemisphere local volume out to a redshift of $\sim$16 000 km s^{-1} (Springob et al. 2014); this volume samples many important attractors including the Shapley supercluster. The velocity field will, in turn, lead to measurements of the local bulk flow on various scales and permit comparisons of the observed velocity field with that predicted from the distribution of galaxies found in redshift surveys (Magoulas et al. in preparation; Scrimgeour et al., in preparation). The 6dFGS redshifts and peculiar velocities will be jointly analysed to characterize the statistical properties of the density and velocity fields captured by the galaxy–galaxy, galaxy–velocity and velocity–velocity power spectra (Johnson et al. 2014; Koda et al., in preparation), providing better determinations of cosmological parameters, such as the redshift space distortion (β) and the correlation between galaxies and dark matter (r_g), that are degenerate given only the information provided by redshift surveys.

In the future, the southern 6dFGSv sample will be combined with the northern SDSS FP sample to recover the local velocity field over about three-quarters of the sky. Comparisons with new all-sky Tully–Fisher (TF) peculiar velocity samples, such as the ongoing 2MASS TF survey (Masters, Springob & Huchra 2008; Hong et al. 2013a,b) and the planned WALLABY/WNSHS surveys (Duffy, Moss & Staveley-Smith 2012a; Duffy et al. 2012b), and with new supernova surveys (e.g. Turnbull et al. 2012; Ma & Scott 2013; Rathaus, Kovetz & Itzhaki 2013), will provide independent cross-checks and refined measurements. Together, these peculiar velocity surveys of thousands of galaxies will provide a clear picture of the motions in the local universe. This will complement the detailed density maps provided by redshift surveys and lead to tighter constraints on a wide range of cosmological parameters.

ACKNOWLEDGEMENTS

We acknowledge the efforts of the staff of the Australian Astronomical Observatory (AAO), who developed the 6dF instrument and carried out the observations for the survey. This publication makes use of data products from the Two Micron All Sky Survey, which is a joint project of the University of Massachusetts and the Infrared Processing and Analysis Center/California Institute of Technology, funded by the National Aeronautics and Space Administration and the National Science Foundation. This research has also made use of the NASA/IPAC Extragalactic Database (NED), which is operated by the Jet Propulsion Laboratory, California Institute of Technology, under contract with the National Aeronautics and Space Administration. JRL acknowledges support from STFC via ST/I001573/1. DHJ acknowledges support from Australian Research Council Discovery Projects Grant DP-0208876, administered by the Australian National University. CM and JM acknowledge support from ARC Discovery Projects Grant DP-1092666. CM was also supported by a scholarship from the Australian Astronomical Observatory. We thank the anonymous referee for providing us with constructive and insightful comments which helped improve this manuscript.

REFERENCES

Adelman-McCarthy J. K. et al., 2008, ApJS, 175, 297
Aihara H. et al., 2011, ApJS, 193, 29
Alonso M. V., Bernardi M., da Costa L. N., Wegner G., Willmer C. N. A., Pellegrini P. S., Maia M. A. G., 2003, AJ, 125, 2307
Bamford S. P. et al., 2009, MNRAS, 393, 1324
Bernardi M. et al., 2003, AJ, 125, 1817
Brough S. et al., 2013, MNRAS, 435, 2903
Burkey D., Taylor A. N., 2004, MNRAS, 347, 255
Burstein D., Davies R. L., Dressler A., Faber S. M., Stone R. P. S., Lynden-Bell D., Terlevich R. J., Wegner G., 1987, ApJS, 64, 601
Cappellari M., Emsellem E., 2004, PASP, 116, 138
Colless M., Hewett P., 1987, MNRAS, 224, 453
Colless M. et al., 2001, MNRAS, 328, 1039
D'Onofrio M. et al., 2008, ApJ, 685, 875
da Costa L. N., Bernardi M., Alonso M. V., Wegner G., Willmer C. N. A., Pellegrini P. S., Rité C., Maia M. A. G., 2000, AJ, 120, 95
Davies R. L., Burstein D., Dressler A., Faber S. M., Lynden-Bell D., Terlevich R. J., Wegner G., 1987, ApJS, 64, 581
de Vaucouleurs G., 1959, Handbuch Phys., 53, 275
de Vaucouleurs G., de Vaucouleurs A., Corwin J. R., eds, 1976, Second Reference Catalogue of Bright Galaxies. Univ. Texas Press, Austin, p. 0
Djorgovski S., Davis M., 1987, ApJ, 313, 59
Dressler A., 1980, ApJS, 42, 565
Dressler A., Lynden-Bell D., Burstein D., Davies R. L., Faber S. M., Terlevich R., Wegner G., 1987, ApJ, 313, 42
Duffy A. R., Moss A., Staveley-Smith L., 2012a, Publ. Astron. Soc. Aust., 29, 202
Duffy A. R., Meyer M. J., Staveley-Smith L., Bernyk M., Croton D. J., Koribalski B. S., Gerstmann D., Westerlund S., 2012b, MNRAS, 426, 3385
Erdoğdu P. et al., 2006, MNRAS, 373, 45
Fernández Lorenzo M., Cepa J., Bongiovanni A., Pérez García A. M., Ederoclite A., Lara-López M. A., Pović M., Sánchez-Portal M., 2011, A&A, 526, A72
Fukugita M. et al., 2007, AJ, 134, 579
Gargiulo A. et al., 2009, MNRAS, 397, 75
Hambly N. C. et al., 2001, MNRAS, 326, 1279
Hong T., Staveley-Smith L., Masters K., Springob C., Macri L., Koribalski B., Jones H., Jarrett T., 2013a, in de Grijs R., ed., Proc. IAU Symp. 289, Advancing the Physics of Cosmic Distances. Cambridge Univ. Press, Cambridge, p. 312
Hong T. et al., 2013b, MNRAS, 432, 1178
Hubble E. P., 1926, ApJ, 64, 321
Hudson M. J., Lucey J. R., Smith R. J., Schlegel D. J., Davies R. L., 2001, MNRAS, 327, 265
Hudson M. J., Smith R. J., Lucey J. R., Branchini E., 2004, MNRAS, 352, 61
Jarrett T. H., 2000, PASP, 112, 1008
Jarrett T. H., Chester T., Cutri R., Schneider S., Skrutskie M., Huchra J. P., 2000, AJ, 119, 2498
Johnson A. et al., 2014, preprint (arXiv:1404.3799)
Jones D. H. et al., 2004, MNRAS, 355, 747
Jones D. H., Saunders W., Read M., Colless M., 2005, Publ. Astron. Soc. Aust., 22, 277
Jones D. H. et al., 2009, MNRAS, 399, 683
Jorgensen I., Franx M., Kjaergaard P., 1995a, MNRAS, 273, 1097
Jorgensen I., Franx M., Kjaergaard P., 1995b, MNRAS, 276, 1341
Korn A. J., Maraston C., Thomas D., 2005, A&A, 438, 685
Lavaux G., Hudson M. J., 2011, MNRAS, 416, 2840
Lavaux G., Tully R. B., Mohayaee R., Colombi S., 2010, ApJ, 709, 483
Lintott C. J. et al., 2008, MNRAS, 389, 1179

Lucey J. R., Carter D., 1988, MNRAS, 235, 1177
Lucey J. R., Guzman R., Carter D., Terlevich R. J., 1991, MNRAS, 253, 584
Lynden-Bell D., Faber S. M., Burstein D., Davies R. L., Dressler A., Terlevich R. J., Wegner G., 1988, ApJ, 326, 19
Magoulas C. et al., 2012, MNRAS, 427, 245
Ma Y.-Z., Scott D., 2013, MNRAS, 428, 2017
Masters K. L., Springob C. M., Huchra J. P., 2008, AJ, 135, 1738
Moore S. A. W., Lucey J. R., Kuntschner H., Colless M., 2002, MNRAS, 336, 382
Pahre M. A., 1999, ApJS, 124, 127
Peng C. Y., Ho L. C., Impey C. D., Rix H.-W., 2010, AJ, 139, 2097
Persson S. E., Frogel J. A., Aaronson M., 1979, ApJS, 39, 61
Proctor R. N., Sansom A. E., 2002, MNRAS, 333, 517
Proctor R. N., Lah P., Forbes D. A., Colless M., Couch W., 2008, MNRAS, 386, 1781
Rathaus B., Kovetz E. D., Itzhaki N., 2013, MNRAS, 431, 3678
Saglia R. P., Burstein D., Baggley G., Davies R. L., Bertschinger E., Colless M. M., McMahan R. K., Jr, Wegner G., 1997, MNRAS, 292, 499
Sánchez-Blázquez P. et al., 2006, MNRAS, 371, 703
Sandage A., 1961, The Hubble Atlas of Galaxies. Carnegie Institution, Washington, DC
Saunders W., Cannon R., Sutherland W., 2004, Anglo-Australian Observatory Epping Newsletter, 106, 16
Schlafly E. F., Finkbeiner D. P., 2011, ApJ, 737, 103
Schlegel D. J., Finkbeiner D. P., Davis M., 1998, ApJ, 500, 525
Simien F., de Vaucouleurs G., 1986, ApJ, 302, 564
Skrutskie M. F. et al., 1997, in Garzon F. et al., eds, Astrophysics and Space Science Library, Vol. 210, The Two Micron All Sky Survey (2MASS): Overview and Status, The Impact of Large Scale Near-IR Sky Surveys. Kluwer, Dordrecht, p. 25
Smith R. J. et al., 2004, AJ, 128, 1558
Springob C. M. et al., 2012, MNRAS, 420, 2773
Springob C. M. et al., 2014, MNRAS, in press
Tonry J., Davis M., 1979, AJ, 84, 1511 (TD79)
Turnbull S. J., Hudson M. J., Feldman H. A., Hicken M., Kirshner R. P., Watkins R., 2012, MNRAS, 420, 447
Watson F. G., Parker Q. A., Miziarski S., 1998, in D'Odorico S., ed., Proc. SPIE Conf. Ser. Vol. 3355, Optical Astronomical Instrumentation. SPIE, Bellingham, p. 834
Wegner G. et al., 2003, AJ, 126, 2268
Zaroubi S., Branchini E., 2005, MNRAS, 357, 527

SUPPORTING INFORMATION

Additional Supporting Information may be found in the online version of this article:

Table 2. 6dFGSv velocity dispersion catalogue.
Table 4. 6dFGSv 2MASS photometric parameters.
Table 8. The 6dFGS FP catalogue.
Table 9. 6dFGS stellar population catalogue (http://mnras.oxfordjournals.org/lookup/suppl/doi:10.1093/mnras/stu1198/-/DC1).

Please note: Oxford University Press is not responsible for the content or functionality of any supporting materials supplied by the authors. Any queries (other than missing material) should be directed to the corresponding author for the paper.

This paper has been typeset from a TEX/LATEX file prepared by the author.